



저작자표시-비영리-동일조건변경허락 2.0 대한민국

이용자는 아래의 조건을 따르는 경우에 한하여 자유롭게

- 이 저작물을 복제, 배포, 전송, 전시, 공연 및 방송할 수 있습니다.
- 이차적 저작물을 작성할 수 있습니다.

다음과 같은 조건을 따라야 합니다:



저작자표시. 귀하는 원저작자를 표시하여야 합니다.



비영리. 귀하는 이 저작물을 영리 목적으로 이용할 수 없습니다.



동일조건변경허락. 귀하가 이 저작물을 개작, 변형 또는 가공했을 경우에는, 이 저작물과 동일한 이용허락조건하에서만 배포할 수 있습니다.

- 귀하는, 이 저작물의 재이용이나 배포의 경우, 이 저작물에 적용된 이용허락조건을 명확하게 나타내어야 합니다.
- 저작권자로부터 별도의 허가를 받으면 이러한 조건들은 적용되지 않습니다.

저작권법에 따른 이용자의 권리는 위의 내용에 의하여 영향을 받지 않습니다.

이것은 [이용허락규약\(Legal Code\)](#)을 이해하기 쉽게 요약한 것입니다.

[Disclaimer](#)

Ph.D. DISSERTATION

**Study on the photo-bias stability for the Zn-Sn-O
field effect transistors**

by

Bong Seob Yang

August 2012

**Department of Materials Science and Engineering
College of Engineering
Seoul National University**

Study on the photo-bias stability for the Zn-Sn-O field effect transistors

Advisor : Prof. Hyeong Joon Kim

By

Bong Seob Yang

A thesis submitted to the Graduate Faculty of Seoul National
University in partial fulfillment of the requirements for the
Degree of Doctor of Philosophy

Department of Materials Science and Engineering

August 2012

Approved

by

Chairman of Advisory Committee : Cheol Seong Hwang

Vice-chairman of Advisory Committee : Hyeong Joon Kim

Advisory Committee : Seungwu Han

Advisory Committee : Myung Soo Huh

Advisory Committee : Jae Kyeong Jeong



Abstract

Recently, novel flexible display and active matrix flat panel displays (FPDs) has received a lot of attention for high definition optical devices. Transparent oxide semiconductor (TOS) materials are especially promising for the channel layer of field-effect transistors (FETs), which are the unit pixel driver for displays, because of their high mobility, good transparency and low processing capability compared to conventional amorphous Si FETs. However, the device reliability against a gate bias stress or/and light stress still remains a critical issue for the implementation of oxide FETs to commercial electronic products.

In this research, the threshold voltage instability of Zinc-Tin oxide based TFTs investigated under the negative bias illumination stress (NBIS) condition and then changed several experimental variables to improve the negative bias illumination stress stability of TFTs.

In this dissertation, thin film transistors (TFTs) with multi-component Zn-Sn-Zr-O (ZTZO) channel layers were fabricated using the co-sputtering method. The incorporation of ZrO₂ into the Zn-Sn-O (ZTO) films led to the degradation of the transport properties. In contrast, the threshold voltage shift under negative bias illumination stress was largely improved. From the XPS results, this improvement was partially attributed to the reduction of the oxygen vacancy defects in the ZTZO film, suggesting that the photo-induced transition from V_O to V_O²⁺ was responsible for the NBIS-

induced instability. Diminishing the $[V_O]$ portion by ZrO_2 incorporation is related to the fact that the Gibbs free energies of formation (ΔG_f). ZrO_2 has the most negative ΔG_f value of ZrO_2 and the chemical bonding with respect to oxygen atoms is the strongest among the Zn, Sn and Zr cation atoms. Thus, increasing the Zr content in the ZTO system will decrease the concentration of V_O . In addition, the photo-desorption mechanism can also be considered as a reason for the V_{th} shift under instability stress conditions. The change in surface coverage with OH groups can affect the number of desorbed oxygen species on the ZTO surface during instability stress duration. This suggests that the surface region of ZTO films is an important factor determining the photo-bias stability of metal oxide TFTs.

The effect of O_3 treatment on the instability of the ZTO TFTs under NBIS conditions was investigated. The O_3 treated device exhibited the much superior stability under NBIS conditions with increasing O_3 treatment time. To understand the effect of O_3 treatment, the chemical state of the O_3 treated ZTO thin film was analyzed systematically by X-ray photoelectron spectroscopy (XPS) and Fourier transformed infrared (FTIR) spectroscopy in absorption mode and contact angle analyzer (CA). The V_O concentration in the ZTO thin film decreased gradually with increasing O_3 treatment time. This suggests that the V_{th} shift of ZTO films under NBIS conditions is due partly to the transition of V_O to V_O^{2+} by light excitation. Therefore, an O_3 treatment can enhance the in-diffusion of oxygen radicals and reduce the $[V_O]$ defect density

in the ZTO film, resulting in an improvement in photo-bias reliability. Simultaneously, the number of hydroxyl groups on the surface of the ZTO film increased with increasing O₃ treatment time. This suggests another reason for the improved NBIS stability of ZTO FETs: the substitution of weakly bound O₂⁻ species at the surface V_O defect sites with OH⁻. This suggests that the surface condition of ZTO films is an important factor determining the photo-bias stability of metal oxide FETs.

Finally, relative contribution of two degradation mechanisms to the overall NBIS-induced V_{th} instability is estimated. In estimation, two types of encapsulated devices with Al₂O₃ film and polymer were prepared to prevent the photo induced adsorption and desorption of O₂⁻ ions from the ZTO surface. Around 85% ~ 90% decrease in the V_{th} shift from the two types of encapsulated devices, compared to that of unpassivated sample, indicates that photo-desorption of oxygen atoms was the dominant factor to cause instability in ZTO based TFTs.

Keywords : Zinc Tin Oxide (ZTO), Zirconium oxide, field effect transistor, photo-bias stability, Negative bias illumination stability (NBIS), ozone treatment

Student ID : 2007-20722

Bong Seob Yang

Table of Contents

Abstract	i
Table of Contents	iv
List of Figures	vii
List of tables	xii
1. Introduction	1
1.1 Overview.....	1
2. Literature Review	9
2.1 Oxide semiconductor Thin-film transistors.....	9
2.1.1 Device structure.....	9
2.1.2 Operation of Thin-film transistors.....	12
2.1.3 Thin film transistor characterization.....	15
2.2 Stability of the oxide TFTs.....	20
3. Experiments and Analyses	31
3.1 Sputter deposition of Oxide films.....	31
3.2 Deposition of ZTO and ZTZO films.....	31
3.3 Thin film transistor Fabrication.....	36
3.4 Analysis Methods.....	41

3.5 Electrical and Reliability Measurements.....	43
4. The effect of bias illumination stress on the TFT reliability.....	45
4.1 Role of ZrO ₂ incorporation in the suppression of negative bias illumination-induced instability in Zn-Sn-O thin film transistors	45
4.1.1 Introduction.....	45
4.1.2 Experimental.....	48
4.1.3 Results and Discussions.....	50
4.1.4 Summary.....	74
4.2 Improvement of the photo-bias stability of the Zn-Sn-O field effect transistors by an ozone treatment.....	76
4.2.1 Introduction.....	76
4.2.2 Experimental.....	78
4.2.3 Results and Discussions.....	81
4.2.4 Summary.....	112
5. Conclusions.....	113
References.....	116

Curriculum vitae	125
List of publications	127
Abstract (in Korean)	135

List of Figures

Fig. 2.1.1. Schematics showing some of the most conventional TFT structures.

Fig. 2.1.2. Comparison between the typical structures of MOSFETs and TFTs.

Fig. 2.1.3. Representative (a) transfer and output characteristics of ZTO based-TFTs

Fig. 2.2.1. Schematic cross section of the TFT and illumination path by the backlight.

Fig. 2.2.2. Linear transfer I_{DS} - V_{GS} curve of a-IGZO TFTs as a function of stress time. The inset shows the bias-stress-induced shift of $\log_{I_{DS}}$ - V_{GS} curve.

Fig. 2.2.3. Evolution of the transfer characteristics of ZnO TFTs under positive or negative gate bias stress with/without light. 41

Fig. 2.2.4. Evolution of the transfer characteristics of the (a) SiN_x/HfO/HIZO, (b) SiN_x/HIZO, and (c) SiN_x/SiO_x/HIZO devices as a function of the NBTIS time. (d) V_{TH} shift as a function of the applied NBITS time for the HIZO TFT with various gate dielectric materials and structures.48

Fig. 2.2.5. Schematic band diagram, which is based on trapping or/and injection of a photo induced hole carrier. 48

Fig. 2.2.6. Schematic band diagram, which is based on transition of neutral oxygen vacancy [V_O] to [V_O^{2+}] charged state by photon irradiation.

Fig. 2.2.7. Schematic summary of the potential instabilities in the AOS TFTs.

Fig. 3.1.1. The sputtering system, (a) an total image of sputtering equipment and (b) enhanced magnetic field structure of cathode (right) compared to the general type (left).

Fig. 3.3.1. Thin film transistor Fabrication process flow.

Fig. 3.3.2. The schematically illustrated structure of TFTs; (a) ITO/channel /SiO₂/p⁺-Si and (b) encapsulating layer/ITO/channel/SiO₂/p⁺-Si.

Fig. 3.3.3. The top-view image of TFTs; (a) ITO/channel /SiO₂/p⁺-Si and (b) encapsulating layer/ITO/channel/SiO₂/p⁺-Si.

Fig. 3.5.1. Schematic diagram of the illumination system.

Fig. 4.1.1. AFM images (2 μm × 2 μm) of post-annealed (a) ZTO and (b) Zn_{0.54}Sn_{0.42}Zr_{0.04}O thin films.

Fig. 4.1.2. X-ray diffraction patterns of the post-annealed ZTO and Zn_{0.54}Sn_{0.42}Zr_{0.04}O thin films.

Fig. 4.1.3. The X-ray reflectivity spectrum for the post-annealed ZTO (line) and Zn_{0.54}Sn_{0.42}Zr_{0.04}O (dashed) thin films.

Fig. 4.1.4. Representative transfer characteristics of TFTs with (a) ZTO and (b) Zn_{0.54}Sn_{0.42}Zr_{0.04}O channel layers.

Fig. 4.1.5. Variations of the transfer characteristics as a function of the applied stress time with ZTO and Zn_{0.54}Sn_{0.42}Zr_{0.04}O (ZTZO) channel layers; (a) NBS of ZTO, (b) NBS of ZTZO, (c)NBIS of ZTO, (d) NNBIS of ZTZO.

Fig. 4.1.6. Variations in V_{th} value as a function of the applied stress time for ZTO and $Zn_{0.54}Sn_{0.42}Zr_{0.04}O$ TFTs; (a) Dark-NBS condition, (b) NBIS condition.

Fig. 4.1.7. Comparison of the SS variations for the ZTO and ZTZO devices under the (a) Dark- NBS condition, (b) NBIS condition.

Fig. 4.1.8. Variations of the transfer characteristics as a function of the applied stress time with ZTO and $Zn_{0.54}Sn_{0.42}Zr_{0.04}O$ (ZTZO) channel layers; (a) PBS of ZTO, (b) PBS of ZTZO, (c)PBIS of ZTO, (d) PNBIS of ZTZO.

Fig. 4.1.9. Variations in V_{th} value as a function of the applied stress time for ZTO and $Zn_{0.54}Sn_{0.42}Zr_{0.04}O$ TFTs; (a) Dark-PBS condition, (b) PBIS condition.

Fig. 4.1.10. The results of TLM measurements; (a) the device structure, (b) the design of TLM patterns. (c) Gate voltage dependence of the total resistance Variations of ZTO film. (d) The width-normalized R_C variation in the fabricated TFTs as a function of the Zr content.

Fig. 4.1.11. XPS O $1s$ spectra and de-convolution results for the (a) ZTO, (b) $Zn_{0.57}Sn_{0.42}Zr_{0.008}O$ and (c) $Zn_{0.54}Sn_{0.42}Zr_{0.04}O$ thin films.

Fig. 4.1.12. XPS O $1s$ spectra and de-convolution results in bulk region for the (a) ZTO, (b) $Zn_{0.57}Sn_{0.42}Zr_{0.008}O$ and (c) $Zn_{0.54}Sn_{0.42}Zr_{0.04}O$ thin films.

Fig. 4.1.13. Variations in contact angle of water droplets of ZTO films with different Zr doping ratio.

Fig. 4.2.1. Representative transfer characteristics of ZTO FETs with (a) untreated, (b) 30 s ozone treated, (c) 300 s ozone treated, and (d) 600 s ozone treated.

Fig. 4.2.2. Evolution of the transfer characteristics for (a) untreated, (b) 30 s ozone treated, (c) 300 s ozone treated, and (d) 600 s ozone treated ZTO FETs as a function of the NBIS time.

Fig. 4.2.3. Variations in V_{th} value as a function of the applied stress time for the different ZTO FETs; (a) Dark-NBS condition, (b) NBIS condition.

Fig. 4.2.4. XPS O $1s$ spectra, which were deconvoluted with three sub-peaks, of (a) untreated ZTO film, (b) 30 s ozone treated, (c) 300 s ozone treated, and (d) 600 s ozone treated ZTO films.

Fig. 4.2.5. Depth profiling of O $1s$ XPS spectra of (a) untreated and (b) 300 s ozone treated ZTO films.

Fig. 4.2.6. The evolution of deconvoluted O $1s$ XPS spectra of the untreated ZTO films as a function of XPS etch time.

Fig. 4.2.7. The evolution of deconvoluted O $1s$ XPS spectra of the 300 s-treated ZTO films as a function of XPS etch time.

Fig. 4.2.8. The valence band (VB) XPS of SiO₂ insulator (black line), untreated ZTO film, 30 s ozone treated, 300 s ozone treated, and 600 s ozone treated ZTO films.

Fig. 4.2.9. FTIR spectra of untreated ZTO film, 30 s ozone treated, 300 s ozone treated, and 600 s ozone treated ZTO films.

Fig. 4.2.10. The energy diagram of various oxygen species in the gas phase, adsorbed at the surface and within the lattice of a binary metal oxide.

Fig. 4.2.11. Process occurring on the ZTO surface during the ozone treatment. (a) air annealing (b) vacuum chamber (c) ozone treated ZTO films.

Fig. 4.2.12. Process occurring on the ZTO surface during the NBIS test.

Fig. 4.2.13. Variations in contact angle of water droplets of ZTO films with different O₃ treatment times.

Fig. 4.2.14. AFM images (2 μm × 2 μm) of (a) untreated ZTO film, (b) 30 s ozone treated, (c) 300 s ozone treated, and (d) 600 s ozone treated ZTO films.

Fig. 4.2.15. The X-ray reflectivity spectrum for the ZTO films with different O₃ treatment times.

Fig. 4.2.16. Evolution of the transfer characteristics for (a) the Al₂O₃ passivated and (b) polymer passivated ZTO TFT as a function of the applied NBIS time.

List of tables

Table 1.1.1. Comparison of a-ZTO, a-Si and poly-Si TFTs.

Table 1.1.2. Typical properties of various *n*-type transparent oxide films.

Table 1.1.3. Summary of physical properties of In₂O₃, ZnO and SnO₂.

Table 3.1.1. Process conditions of ZTO films.

Table 3.1.2. Process conditions of ZTZO films.

Table 4.1.1. Best-simulated XRR results for ZTO and Zn_{0.54}Sn_{0.42}Zr_{0.04}O thin films of Fig. 4.1.3.

Table 4.1.2. Device characteristics and Variations in V_{th} value for the ZTO and Zn_{0.54}Sn_{0.42}Zr_{0.04}O FETs.

Table 4.1.3. Comparison of portion of the O 1s peaks deconvoluted from the XPS spectra at the surface of the ZTO-based films.

Table 4.1.4. Comparison of portion of the O 1s peaks deconvoluted from the XPS spectra in the bulk of the ZTO-based films.

Table 4.2.1 Device characteristics and Variations in V_{th} value for the different ZTO FETs

Table 4.2.2. Comparison of portion of the O 1s peaks deconvoluted from the XPS spectra at the surface of the ZTO-based films.

Table 4.2.3. Comparison of portion of the O 1s peaks deconvoluted from the XPS spectra of the untreated and 300 s-treated ZTO films as a function of XPS etch time.

Chapter 1. Introduction

1.1 Overview

Amorphous Si:H and polycrystalline silicon has been used in switching devices, including as thin film transistor (TFT) backplanes for high-end liquid crystal displays (LCDs), transparent organic light emitting diodes (OLEDs). In recent years, amorphous oxide semiconductor (AOS) materials have accelerated the development of field-effect transistors (FETs), which are the unit pixel driver for novel flexible display as well as active matrix flat panel displays for high-end display devices. It is a key technique to fabricate suitable TFTs for achieving the high performance display devices.

The existing channel materials such as a -Si:H,¹ low-temperature polycrystalline silicon (LTPS)² have been used as channel layer materials in TFTs. In the case of LTPS TFTs, there reduce the response time for the operation of high-end display devices³ by higher electron mobility ($\sim 100 \text{ cm}^2/\text{V}\cdot\text{s}$) compared to that of a -Si:H ($\sim 1 \text{ cm}^2/\text{V}\cdot\text{s}$). However, the non-uniform distribution due to the rough surface, grain boundary and grain sizes effect of LTPS are the main causes of the wide distribution in the threshold voltage and mobility in TFTs.^{4,5} In LTPS-used circuits, there must be included the extra circuits to solve the uniformity problems.

Furthermore, the TFTs using a -Si:H channel layer also have unsuitable performance for high-end devices. Above all, the mobility of a -Si:H TFTs is not sufficient. For example, it will suffice for the backplane of small size AMOLEDs by designing the smart pixel circuit and the enhancing the OLED efficiency. However, it is hard to adopt the large area display devices by using a -Si:H TFTs due to the poor mobility. In addition, there are threshold voltage shift of a -Si:H TFTs characteristics, This instability is caused by the metastable nature of a -Si itself. These unstable a -Si:H TFTs are actually well tolerated to the relatively non-demanding AMLCD pixel application. Because of the TFTs are used for voltage control in a simple switching context. In the other hand, the stability of a -Si:H TFTs is inadequate for the TFT backplanes of AMOLEDs working by current control application. According to the result of J. Lee *et. al.*, the threshold voltage of a -Si:H TFT on AMOLEDs is shifted by the stress time.⁶ The comparison of a -ZTO with a -Si and poly-Si was summarized in Table 1.1.1.⁷⁻¹²

In contrast, amorphous oxide semiconductor (AOS) has a merits on the low cost fabrication and a higher mobility than a -Si:H, and it also has easy process and uniformity compared to those based on LTPS. As the result, AOS are considered much more favorable for high-end display devices than other competitor materials. The typical properties of various transparent oxide films were listed in Table 1.1.2.¹³ These transparent conducting oxide films are n -type semiconductors with an optical band-gap energy (E_g^{opt}) of

about 2.2 - 4.3 eV.^{14,15} These transparent conducting properties are sought in a number of applications as electrode materials in solar cells, light emitting diodes, flat panel displays, and other optoelectronic devices where an electric contact needs to be made without obstructing photons from either entering or escaping the optical active area and in transparent electronics such as transparent field-effect transistors.¹⁶⁻¹⁹

In this study, a bottom gate TFT with Zinc and Tin based channel layer was fabricated. This dissertation discussed the threshold voltage instability of Zinc-Tin oxide based TFTs under the negative bias illumination stress and several experimental variables to improve the negative bias illumination stress stability of TFTs. The physical properties of common transparent oxide semiconductor, SnO₂, ZnO and In₂O₃ were listed in Table 1.1.3.²⁰ However, the structure of sputtering deposited oxide thin film can be polycrystalline or amorphous phase, which is highly dependent on the deposition temperature, technique, post-annealing treatment and doping level.¹⁴ The perfect stoichiometric forms of these oxides are good insulator. However, non-stoichiometry, in particular oxygen deficiency, makes it conductor. Kilic and Zunger showed that the formation energy of oxygen vacancies and tin interstitials in SnO₂ is very low and thus these defects form readily.²¹

In this dissertation, Thin film transistors (TFTs) with In and Ga-free multi-component Zn-Sn-Zr-O (ZTZO) channel layers were fabricated

using the co-sputtering approach. The incorporation of ZrO_2 into the Zn-Sn-O (ZTO) films led to the degradation of the transport properties. In contrast, the threshold voltage shift under negative bias illumination stress was largely improved. This improvement was attributed to the reduction of the oxygen vacancy defects in the ZTZO film, suggesting that the photo-induced transition from V_O to V_O^{2+} was responsible for the NBIS-induced instability. In addition, the photo-desorption mechanism can also be considered as a reason for the V_{th} shift under instability stress conditions. The change in surface coverage with OH groups can affect the number of desorbed oxygen species on the ZTO surface during instability stress duration. This suggests that the surface region of ZTO films is an important factor determining the photo-bias stability of metal oxide TFTs.

In addition, the effect of O_3 treatment on the instability of the ZTO FETs using a NBIS test was studied. The O_3 treated device exhibited the much superior stability under NBIS conditions with increasing O_3 treatment time. The chemical state of the O_3 treated ZTO thin film was analyzed systematically by XPS, FTIR and contact angle measurements. The improvement in NBIS stability of the O_3 treated ZTO FETs was related to the lower oxygen vacancy concentration and retarded desorption of adsorbed oxygen under photon irradiation by the O_3 treatment. And the possible reasons for such stable behavior of stability are also discussed in detail.

The organization of this dissertation is as follows. Chapter 2

reviews literature of general information on transparent oxide semiconductors, thin-film transistors and explained the TFT device structure and characterization. Chapter 3 explained the device fabrication processing and analysis methods. Chapter 4 presents the effect of light on the electrical property of Zinc-Tin oxide-based TFTs under negative bias stress. Chapter 5 provides the conclusion of the thesis.

Table 1.1.1. Comparison of a-ZTO, a-Si and poly-Si TFTs [7-12].

Property	a-ZTO	a-Si	poly-Si
μ_{SAT} (cm ² /V·s)	~ 20	< 1	30 ~ 100
ΔV_{TH}	- 0.5 V	< 3 V	< 1×10 ⁻² V
S (V/decade)	0.5	1.49	0.5
Process Temp. [°C]	RT ~ 400	150 ~ 350	250 ~ 550
TFT uniformity	Good	Good	Poor
TFT type	n-type	n-type	CMOS
Application	AMLCD, AMOLED	AMLCD	AMOLED

Table 1.1.2. Typical properties of various *n*-type transparent oxide films [13].

Mat.	E_g^{opt} (eV)	T (%)	μ_{Hall} (cm ² /Vs)	N_d (cm ⁻³)	ρ (Ω cm)
CdO	2.2-2.6	75	220	10 ¹⁹ - 10 ²¹	2×10 ⁻³
Cd ₂ SnO ₄	2.9-3.1	90	35-60	~7×10 ²¹	~2×10 ⁻⁴
In ₂ O ₃	3.7	80-90	10-40	≤ 10 ²¹	≥ 10 ⁻⁴
InGaO ₃	3.3	90	10	10 ²⁰	2.5×10 ⁻³
InGaZnO ₄	3.5	80-90	24	~10 ²⁰	2×10 ⁻³
SnO ₂	3.6	80-90	5-30	≤ 10 ²⁰	≥ 10 ⁻³
ZnO	3.2-3.3	80-90	5-50	≤ 10 ²¹	≥ 10 ⁻⁴
Zn ₂ In ₂ O ₅	2.9	80	12-20	~5×10 ²⁰	4×10 ⁻³
ZnSnO ₃	3.5	80	7-12	10 ²⁰	5×10 ⁻³
Zn ₂ SnO ₄	3.3-3.9	90	12-26	6×10 ¹⁸	~5×10 ⁻²

※ E_g^{opt} : optical band-gap, χ : electron affinity, μ_{Hall} : Hall mobility, N_d : carrier concentration, ρ : resistivity

Table 1.1.3. Summary of physical properties of In₂O₃, ZnO and SnO₂ [20].

Property	In ₂ O ₃	ZnO	SnO ₂
Mineral name	-	Zincite	Cassiterite
Abundance of the metal in the earth's crust (ppm)	0.1	132	40
Crystal structure	Cubic, bixbyite	Hexagonal, wurtzite	Tetragonal, rutile
Lattice constants [nm]	$a = 1.012$	$a = 0.325$ $b = 0.521$	$a = 0.474$ $b = 0.391$
Density [g cm ⁻³]	7.12	5.67	6.99
Thermal expansion coefficient (300K) [10 ⁻⁶ K ⁻¹]	6.7	∥ c: 2.92 ⊥ c: 4.75	∥ c: 3.7 ⊥ c: 4.0
Melting point [°C]	2190	2240	>1900
Static dielectric constant	~9	∥ c: 8.75 ⊥ c: 7.8	∥ c: 9.6 ⊥ c: 13.5
Refractive index		2.008	
E_g^{opt} [eV]	3.75	3.4	3.6
Intrinsic N_d		$< 10^6$ cm ⁻³	
Exciton binding energy		60 meV	
Electron Hall mobility	200 cm ² V ⁻¹ s ⁻¹	200 cm ² V ⁻¹ s ⁻¹	
Hole Hall mobility	5-50 cm ² V ⁻¹ s ⁻¹	5-50 cm ² V ⁻¹ s ⁻¹	

Chapter 2. Literature Review

2.1 Oxide semiconductor Thin-film transistors

2.1.1 Device structure

During thin film transistor process, each composition layer is prepared by thin film deposition method like CVD and sputter, therefore there is a great degree of freedom on the deposition sequence of channel layer and electrodes.²² Figure 2.1.1 shows the most typical structure of TFTs.^{22,23} In staggered structure, The source/drain are on opposite of semiconductor. While source/drain are place on the same side of semiconductor for the coplanar structure. The staggered structure are normally used in a-Si:H TFT. The staggered bottom gate structure is used in poly-Si TFT and a-Si:H TFT in LCDs. Because of the gate metal electrode screens the channel layer from the degradation effect of the back light. The coplanar structure is unusual cases for the a-Si:H TFT. Each of these structures is selected by advantage of process integration issues, easier processing and enhanced electrical properties.^{24,25} In this study, the bottom gate structure used because the channel layer is exposed to air, it is easily modify the channel layer properties, the chemical adsorption/desorption on the back surface during annealing or additional treatment. During deposition

process, other layers can be added for different purposes. For example, an insulating film is often deposited on top of the channel layer in bottom gate structures. The insulating layer can improve accurate etching of the channel layer, without damaging the semiconductor surface as an etch-stopper.²⁶ This insulating layer on top of the TFT can act as an effective chemical protection layer of the channel material from environmental species such as moisture and oxygen, which can be an electron source, and the conductivity of channel material could be changed.^{27,28}

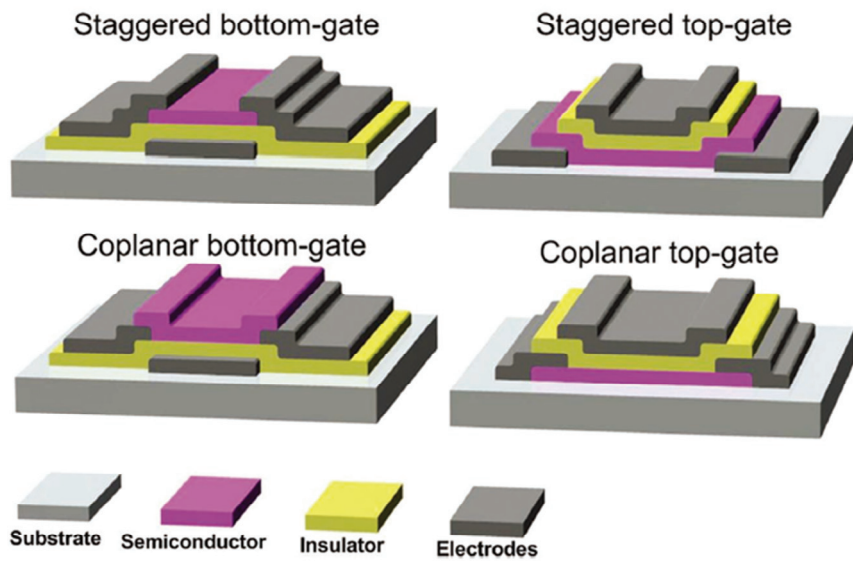


Fig. 2.1.1. Schematics showing some of the most conventional TFT structures. [23]

2.1.2 Operation of Thin-film transistors

Thin film transistor (TFT) are similar to Metal oxide semiconductor field effect transistor (MOSFET) used in microprocessors or memories applications in terms of operation and composing layers. However, many differences exist between TFTs and MOSFETS. Figure 2.1.2 shows comparison between the typical structures of TFTs and MOSFETS.²³ First, in MOSFETs the silicon wafer acts as the substrate and the semiconductor layer. While TFTs use an insulating substrate, normally glass and use a deposition material as channel layer. As the result, MOSFET has higher performance, given that the electrons flow in a single crystalline si wafer, rather than in a polycrystalline or amorphous oxide semiconductor. Also, the process temperatures of both devices are quite different. In MOSFET process, for the creation of the dielectric layer, processing temperatures usually exceed over 1000 °C, while in TFTs processing temperatures are limited by the glass substrates, which does not exceed 600 ~ 650 °C.²⁶ In addition, MOSFETs have p-n junctions between the source/drain and channel layer, which are not in TFTs. This is related with another important difference in device characteristics. When the TFTs and MOSFETs rely on the field effect to modulate the conductance of the channel layer on state, in TFTs this is achieved by an accumulation layer. While in MOSFETs, the applied gate bias makes an inversion region in the

channel, then the carrier can flow. Thus in MOSFETs, a n-type conductive depletion layer is created in a p-type silicon wafer substrate.

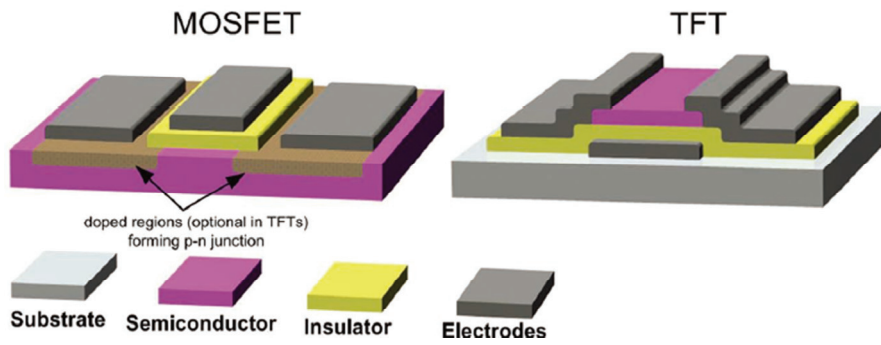


Fig. 2.1.2. Comparison between the typical structures of MOSFETs and TFTs. [23]

2.1.3 Thin film transistor characterization

The TFTs are field effect devices like MOSFETs, the analysis of TFTs devices characterization typically is carried out by using MOSFET drain current equations. Drain current on/off ratio, channel mobility (μ), turn-on voltage (V_{ON}) and threshold voltage (V_{TH}), subthreshold swing (S) are often used for device performance characteristic.

1) Channel mobility (μ)

This is most often used for device characterization Channel mobility is related with the carrier transport in a channel layer, affected by several scattering mechanisms, such as lattice vibrations, ionized impurities, grain boundaries and other structural defects.²⁹ Because of the movement of carriers is constrained to a narrow channel region close to the interface, additional sources of scattering should be considered, such as Coulomb scattering from dielectric charges and surface roughness scattering. The MOSFET equations for thin film transistor are shown following,

in linear region, $V_D < V_G - V_T$

$$I_{D,linear} = \frac{W}{L} \mu_{eff} C_{ox} (V_G - V_T) V_{DS}$$

$$g_m = \left. \frac{\partial I_{DS}}{\partial V_{GS}} \right|_{V_{DS}=\text{const.}} = \frac{W}{L} \mu_{\text{eff}} C_{\text{ox}} V_{DS}$$

Field effect mobility (μ_{FE} or μ_{eff}) is extracted using,

$$\mu_{\text{FE}} = \frac{L g_m}{W C_{\text{ox}} V_{DS}}$$

in saturation region, $V_D > V_G - V_T$

$$I_{D,\text{sat}} = \frac{W \mu_{\text{sat}} C_{\text{ox}}}{2L} (V_G - V_T)^2$$

Saturation mobility (μ_{SAT}) is extracted using,

$$\mu_{\text{sat}} = \frac{2L m^2}{W C_{\text{ox}}}$$

m : slope of $\sqrt{I_{D,\text{sat}}} - (V_G - V_T)$

where L is the channel length, W is the width, and C_{ox} is the gate capacitance per unit area.

2) subthreshold swing (S)

The subthreshold swing are estimated using a log plot of the transfer curve. S is the inverse of the maximum slope in the transfer curve. S can be an useful parameter of how effectively the TFTs turn on by the gate bias.

$$S = \frac{1}{\text{slope}} = \frac{V_2 - V_1}{\log(I_{DS2} - I_{DS1})}$$

3) Drain current on/off ratio

This is a parameter for switching device and defined as the ratio of the on current to off current. Figure 2.1.3 shows the transfer and output characteristics of ZTO based-TFTs using in this study. For in ZTO based-TFT, the on/off ratio is over 10^7 , respectively.

4) Turn-on voltage (V_{ON}) and threshold voltage (V_{TH})

Turn-on voltage and threshold voltage (V_{TH}) has different physical meaning and which can be defined using several methodologies.³⁰ In this study, V_{on}/V_{TH} were defined as the gate voltage which induces a drain current of $L/W \times 10$ nA at $V_{DS} = 10.1$ V.³¹ The extraction of V_{on}/V_{TH} in this way is frequently used because the analog driver in the actual unit pixel of

AMOLED panel is loaded between $1\mu\text{A}$ and 1nA . Here, the roughly $1\mu\text{A}$ and 1nA are needed to embody the full-on and black gray scale for AMOLED devices, respectively. Although this type of V_{th} definition does not have a unique physical meaning, the gate voltage to induce a drain current of 10nA can be a very useful guideline for the panel design as well as the process control.

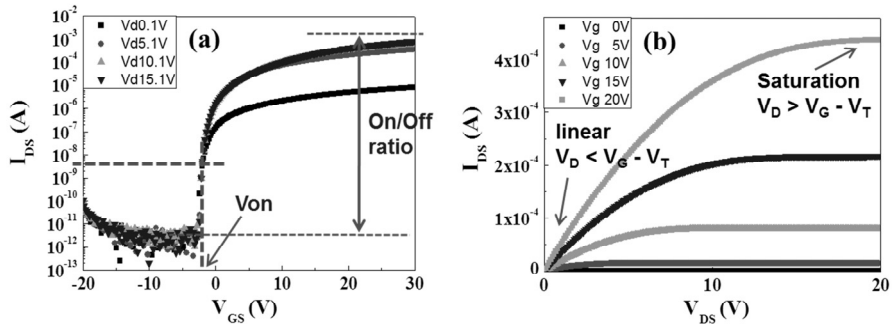


Fig. 2.1.3. Representative (a) transfer and output characteristics of ZTO based-TFTs

2.2 Stability of the oxide TFTs

Metal oxide thin film transistors have strong potential to be used in unit pixel driver for novel flexible display as well as active matrix flat panel displays (FPDs), including as thin film transistor backplanes for high-end liquid crystal displays, transparent organic light emitting diodes and flexible displays, because they provide intriguing properties as compared with amorphous Si (a-Si) semiconductor and polycrystalline Si TFTs, including a high mobility, excellent uniformity, and good transparency to visible light.³² The device reliability against a gate bias stress or/and light stress still remains a critical issues remaining to be resolved before their implementation in commercial electronic products.^{32,33} Figure 2.2.1 shows schematic cross section of the oxide TFT and illumination path by the backlight.³⁴ Figure 2.2.2 shows evolution of the transfer characteristics as a function of the positive bias stress time. The V_{TH} has a parallel shift to the positive direction by positive bias stress without change in mobility and subthreshold slope value.³⁵ The degradation mechanism of positive BTI (PBTI) for metal oxide TFTs has been intensively studied and can be attributed to the trapping of electron carriers accumulated in the channel/insulator interface,³⁶ the creation of defects in the semiconductor material,³⁷ and/or the ambient dynamics of the un-encapsulated back channel region.³⁸ From these results, the PBTI has been improved by optimizing the

gate dielectric and passivation layer.^{31,39,40} In contrast, it was reported that the performance degradation associated with the threshold voltage (V_{th}) is more severe for NBTI than for PBTI under simultaneous light stress. Figure 2.2.3 shows the evolution of the transfer characteristics of ZnO TFTs under positive or negative gate bias stress with/without light.⁴¹ Because the operation of LCDs and transparent displays inevitably suffers from light stress, including that resulting from the back light unit and/or external visible light, the negative bias illumination stress induced instability is still one of the crucial obstacles to their practical application. In this regard, intensive efforts have been made to understand the origin of this NBIS instability. Three degradation models have been reported which can be considered as plausible origins; i) the photo-induced hole trapping,⁴²⁻⁴⁵ ii) photo-transition⁴⁶ from V_O to V_O^{2+} and iii) photo-desorption of O_2 on the channel surface.⁴⁷ As shown in Fig.2.2.5, the hole trapping model assumes that photo-generated hole carriers drift toward the gate insulator by the negative electric field and are trapped at the gate dielectric/channel interfacial trap sites or gate dielectric bulk film.⁴³ Therefore, the hole trapping phenomena depends strongly on the gate dielectric material. Figure 2.2.4 shows the transfer characteristics of the SiNx/HfO/HIZO, SiNx/HIZO, and SiNx/SiOx/HIZO devices as a function of the NBTIS time. And V_{TH} shift as a function of the applied NBITS time for the HIZO TFT with various gate dielectric materials.⁴⁸

Another plausible mechanism was reported that a V_O defect center acts as the source of hole carriers via V_O mediated e-h pair generation during NBIS.⁴⁹ In this model assumes that photo irradiation causes the transition of neutral oxygen vacancies $[V_O]$ to the +2 charge states $[V_O^{2+}]$. The $[V_O]$ forms a deep state and the $[V_O^{2+}]$ state donates two electrons into the conduction band as shown in Fig. 2.2.6. Therefore, under illumination condition, the photo-transition from $[V_O]$ to $[V_O^{2+}]$ can cause an increase free electron carrier density, leading to increase of conductivity of channel layer and a negative V_{th} shift.

The photo-desorption mechanism can also be considered as a possible reason for the negative V_{th} shift under NBIS duration.^{50,51,52} Because the change in surface coverage with oxygen groups on the back channel surface can affect the number of electron in channel layer during NBIS. It is necessary to discuss the plausibility of O_2 photo-desorption on the channel surface. By oxygen adsorption from ambient electron depletion layer are formed on the back channel surface in air ambient. Light-illumination can causes the desorption of oxygen species on the back channel surface. This photo desorption of adsorbed oxygen releases delocalized electrons into the channel layer. As the result, the free electron density will be increased compared to that of the dark state, leading to increase of conductivity of channel layer and a negative V_{th} shift.

In order to verify these models, the effect of ZrO_2 incorporation in

the ZTO film and field effect transistors was investigated and the photo-bias stability of ZTO FETs by performing an ozone treatment was investigated. As similar approaches with ozone treatment, high pressure O₂ annealing and oxygen plasma treatments were demonstrated.^{47,49} However, the present study showed that a simple oxygen vacancy reduction model cannot explain all the experimental observations, and suggested that the surface chemistry of ZTO films related to the chemical adsorption on the back surface of the channel plays a crucial role. And the possible reasons for such highly stable behavior are also discussed in detail.

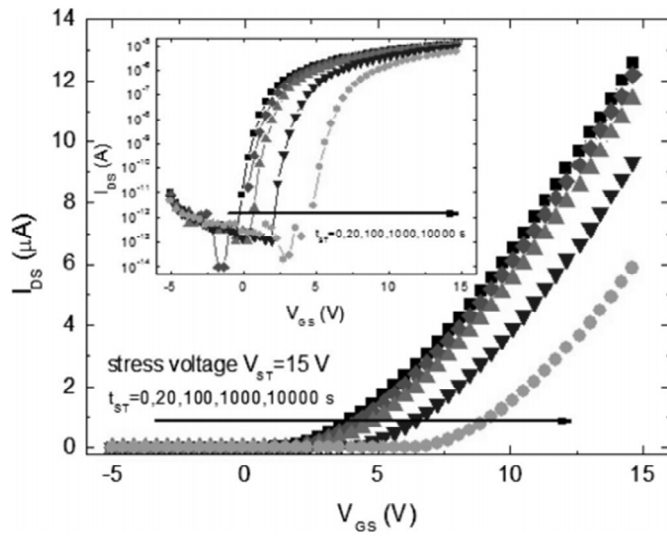


Fig. 2.2.2. Evolution of the transfer characteristics of ZnO TFTs under positive or negative gate bias stress with/without light. [35]

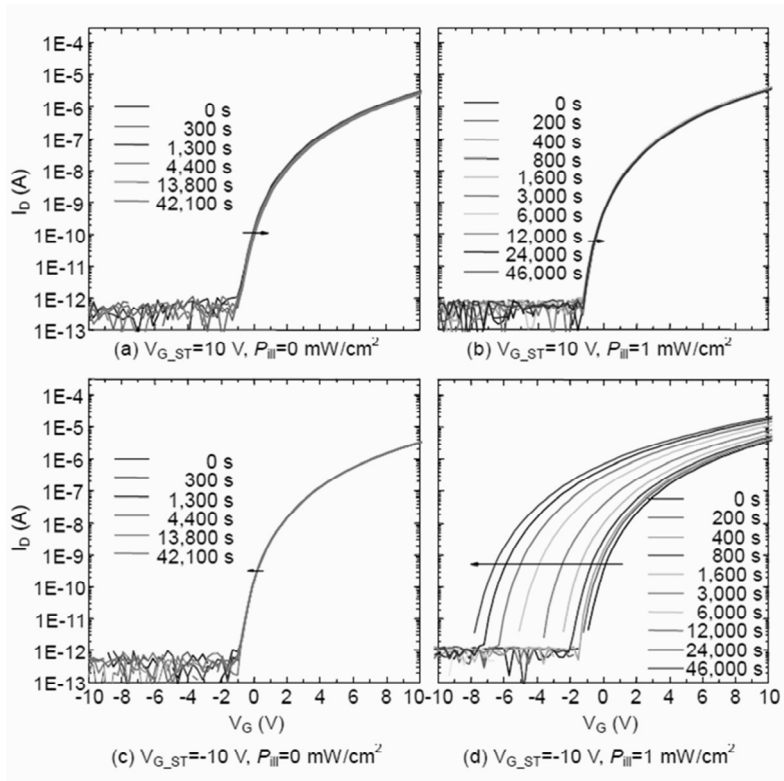


Fig. 2.2.3. Evolution of the transfer characteristics of ZnO TFTs under positive or negative gate bias stress with/without light. [41]

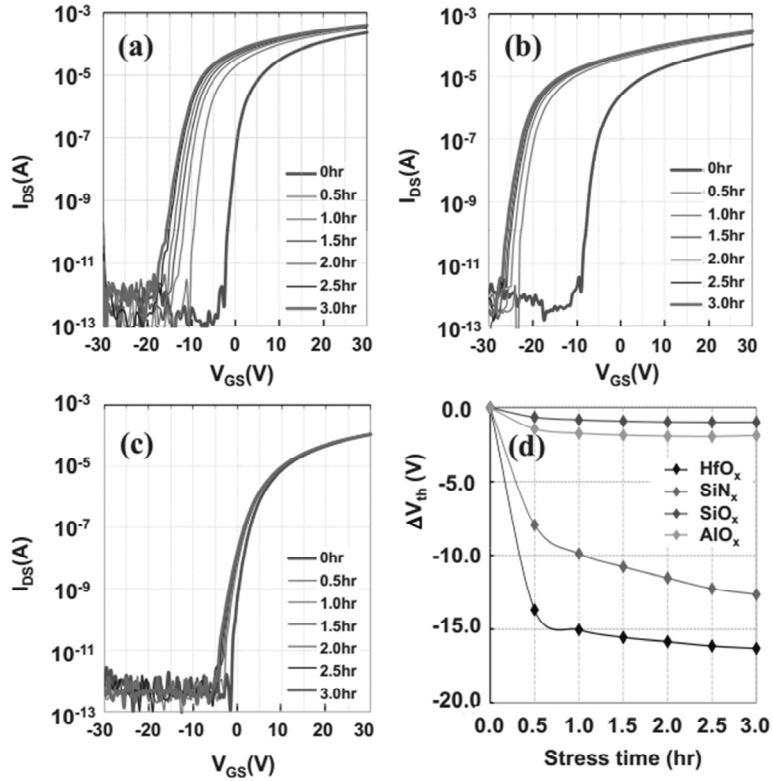


Fig. 2.2.4. Evolution of the transfer characteristics of the (a) SiNx/HfO/HIZO, (b) SiNx/HIZO, and (c) SiNx/SiOx/HIZO devices as a function of the NBTIS time. (d) V_{TH} shift as a function of the applied NBTIS time for the HIZO TFT with various gate dielectric materials and structures. [42]

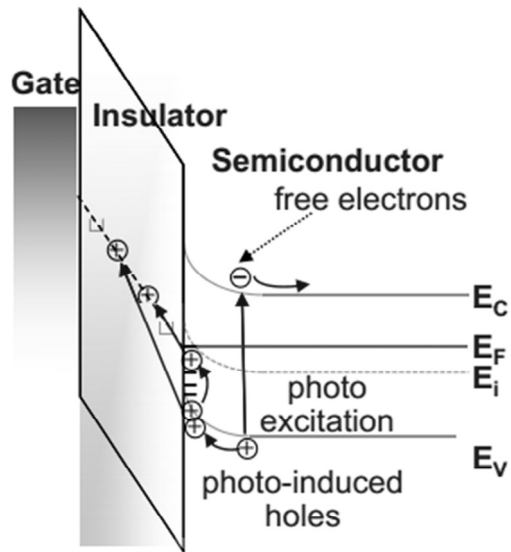


Fig. 2.2.5. Schematic band diagram, which is based on trapping or/and injection of a photo induced hole carrier. [42]

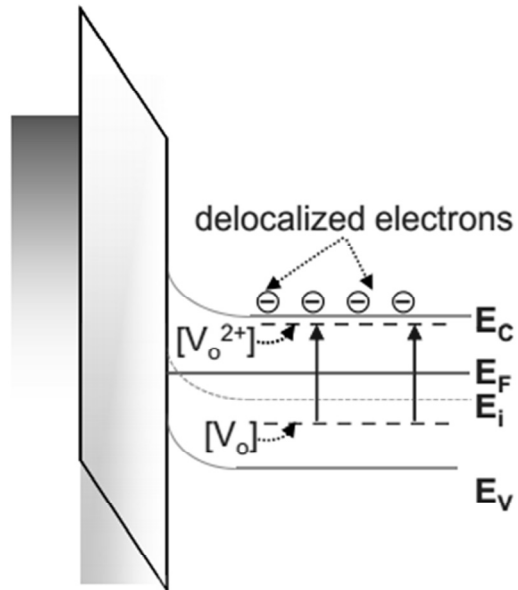


Fig. 2.2.6. Schematic band diagram, which is based on transition of neutral oxygen vacancy $[V_O]$ to $[V_O^{2+}]$ charged state by photon irradiation. [42]

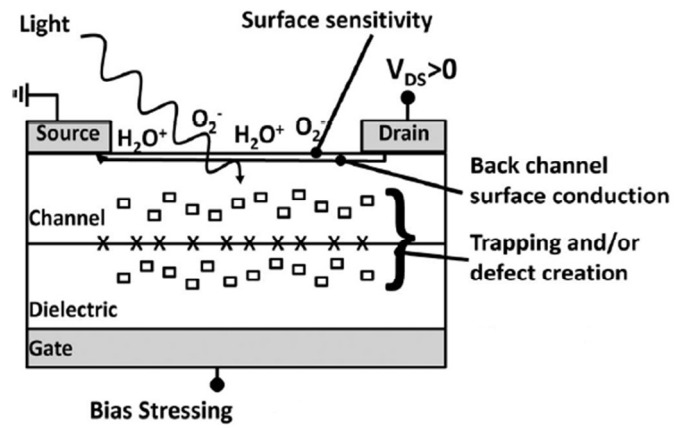


Fig. 2.2.7. Schematic summary of the potential instabilities in the AOS TFTs.

[46]

Chapter 3. Experiments and Analyses

3.1 Sputter deposition of Oxide films

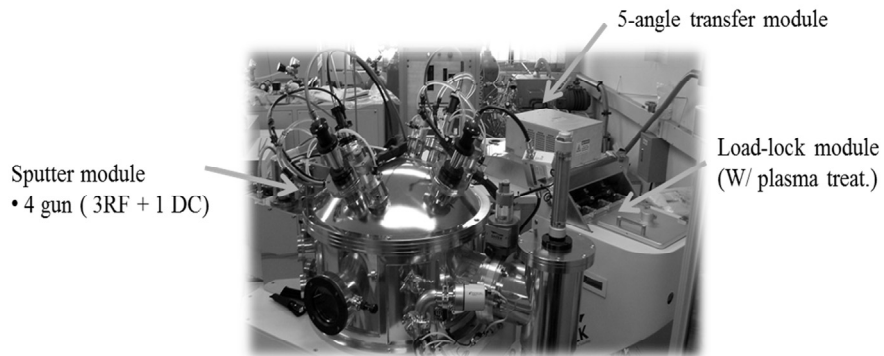
RF/DC magnetron sputtering systems was used for the oxide semiconductor and ITO electrode films deposition. Figure 3.1.1(a) and (b) show the sputtering system (CS5000, SNTek Corp.) constituted with 5-angle cluster-type system and the sputter gun. The cathode of the sputter gun was modified to enhance the magnetic field at the target surface compared to the general type.⁵³ The magnetic housing of the gun cathode was designed to maximize the magnetic field on the target surface and to minimize the distance between the center and edge magnets

3.2 Deposition of ZTO and ZTZO films

In the experiments for chapter 4.1, 36-nm-thick ZTO and ZTZO film were deposited on Si wafers and on highly doped p-type silicon wafers with a 100-nm-thick thermal oxide layer. During deposition, a 3-inch diameter ZnO:SnO₂ (1:1 at%) ceramic target and ZrO₂ (99.99%) target were utilized as the ZTO and ZrO₂ precursors. The input rf power of ZTO target was fixed at 100 W, while that of the ZrO₂ target was varied from 0 W to 100 W at room temperature. The distance between the substrate and the target

was about ~15 cm. The chamber base pressure was below 1.0×10^{-6} Torr. The sputtering was carried out at the chamber pressure of 5 mTorr and the oxygen to Ar (O_2/Ar) gas ratio was 0.3. After the deposition, the samples were annealed in a vertical type quartz tube furnace at a temperature of 350 °C for 1 hour in air ambient. The specifications of detailed deposition conditions for ZTO films and ZTZO films were summarized in Table 3.1.1 and Table 3.1.2.

(a)



(b)

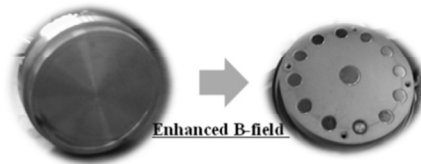


Fig. 3.1.1. The sputtering system, (a) an total image of sputtering equipment and (b) enhanced magnetic field structure of cathode (right) compared to the general type (left).

Table 3.1.1. Process conditions of ZTO films.

	ZTO
Target	ZnO:SnO ₂ (1:1 at%)
Sputtering Power (W)	100
Initial Pressure (Torr)	1.0×10^{-6}
Sputtering Pressure (Torr)	5.0×10^{-3}
Target-Substrate Distance (cm)	~ 15
Substrate Rotation Rate (rpm)	12
Substrate Temperature	Room Temperature
Sputtering Gas Flow (sccm)	Ar = 7
Reactive Gas Flow (sccm)	O ₂ = 3

Table 3.1.2. Process conditions of ZTZO films.

	ZTO	
Target	ZnO:SnO ₂ (1:1 at%)	ZrO ₂ (99.99%)
Sputtering Power (W)	100	0 ~ 100
Initial Pressure (Torr)	1.0 × 10 ⁻⁶	
Sputtering Pressure (Torr)	5.0 × 10 ⁻³	
Target-Substrate Distance (cm)	~ 15	
Substrate Rotation Rate (rpm)	12	
Substrate Temperature	Room Temperature	
Sputtering Gas Flow (sccm)	Ar = 7	
Reactive Gas Flow (sccm)	O ₂ = 3	

3.3 Thin film transistor Fabrication

Zinc-tin oxide based thin film transistors were fabricated by sputtering method. In the experiments for chapter 4.1, 36-nm-thick ZTO and ZTZO channel layers were deposited by reactive RF magnetron sputtering on highly doped p-type silicon wafers with a 100-nm-thick thermal oxide layer. In the experiments for chapter 4.2, 19-nm-thick ZTO channel layer was prepared by same magnetron sputtering system. A highly-doped p-type silicon wafer itself was used as the gate electrode, and high quality thermal SiO₂ film was used as a gate insulator, in order to prevent the injection of charge carriers into the underlying gate dielectric under NBIS conditions.⁴² Then, a 100-nm-thick source/drain electrode composed of tin-doped indium oxide film (In₂O₃ : SnO₂ = 90 : 10 wt %) was formed by the dc sputtering process at room temperature. Argon was used as the sputtering gas and dc power was fixed 100 W at the chamber pressure of 5 mTorr. The channel and source/drain electrodes were patterned using a shadow mask with a channel length of 300 μm and a width of 1000 μm. After the deposition, the samples were annealed in a vertical type quartz tube furnace at a temperature of 350 °C for 1 hour in air ambient. Thin film transistor Fabrication process flow was summarized in Fig. 3.3.1. The Schematics and the top-view images of this structure were shown in Fig. 3.3.2 and Fig. 3.3.3.

In the experiments for chapter 4.2, the ozone (O₃) treatment of ZTO

films was conducted after post-deposition annealing (PDA) as follows: the chamber working pressure was kept at 5 torr; the O₃ treatment was performed at 210 °C and the treatment time was split into 0 s, 30 s, 300 s, and 600 s; and the O₃ flow rate was fixed to 50 g/min, which was generated from 400 sccm of O₂. In addition, two types of encapsulated ZTO TFTs were prepared to prevent the photo induced adsorption and desorption of O₂⁻ ions from the ZTO surface. First, a 13-nm-thick Al₂O₃ film was deposited on the ZTO TFT surface by thermal atomic layer deposition (ALD) with Al(CH₃)₃ and ozone as the Al-precursor and oxygen source, respectively, at a substrate temperature of 210 °C. However, the presence of highly reactive ozone during the ALD process could have affected the bulk defect density of the ZTO channel layer. In order to neglect such effect from the ALD process, the polymer passivation layer on ZTO TFT was formed by a spin coating method.

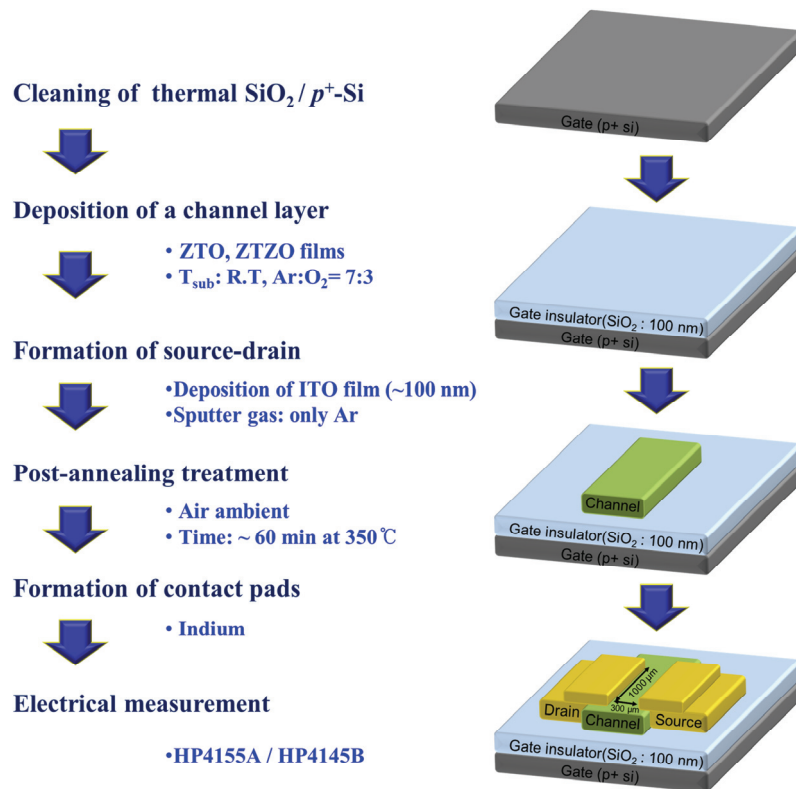


Fig. 3.3.1. Thin film transistor Fabrication process flow.

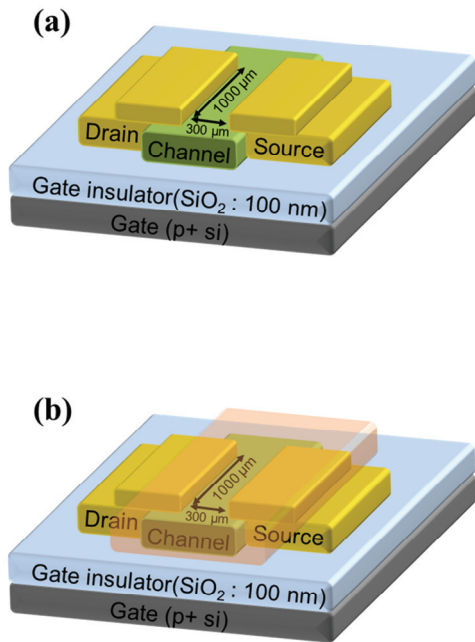


Fig. 3.3.2. The schematically illustrated structure of TFTs; (a) ITO/channel / SiO_2/p^+ -Si and (b) encapsulating layer/ITO/channel/ SiO_2/p^+ -Si.

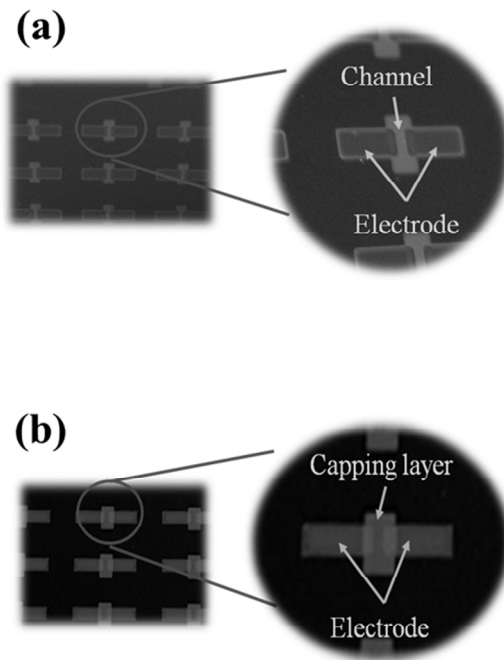


Fig. 3.3.3. The top-view image of TFTs; (a) ITO/channel /SiO₂/p⁺-Si and (b) encapsulating layer/ITO/channel/SiO₂/p⁺-Si.

3.4 Analysis Methods

The thickness of the oxide thin films was measured using an ellipsometer with a fixed refractive index value. The chemical bonding states of the oxide films were examined by X-ray photoelectron spectroscopy (XPS, SIGMA PROBE, Thermo VG, U.K) with a Al $K\alpha$ source (15 kV or better) for the excitation of photoelectrons. To calibrate the photoelectron binding energy, the C $1s$ peak for C-C bonds was assigned to 284.5 eV. The depth profiling of O $1s$ XPS spectra was carried out in order to evaluate the V_O density in bulk region as well. A depth profile using AES was created by sputtering, using accelerated Ar^+ ion. The surface roughness and the surface morphology of the films were investigated by atomic force microscopy (AFM, JEOL, JSPM-5200) in scan lengths of 2.0 μm . The roughness was cross-checked by XRR measurements. Standard Θ - 2Θ and glancing angle incidence X-ray diffraction (XRD, X'Pert-PRO, PANalytical) measurements were performed using Cu $K\alpha$ radiation to evaluate the crystallinity of annealed oxide films. High-resolution X-ray reflectivity (XRR) measurements were performed to determine the roughness, density, and thickness of the ZTO and ZTZO thin films. The XRR data so obtained were fitted using the PANalytical X'Pert Reflectivity software package. To investigate the electrical resistivity, free carrier concentration, and Hall mobility of the films, Hall Effect measurements were carried out using the

van der Pauw configuration.^{29,54} The magnetic field was fixed at 0.5 T. The thermal evaporated aluminium electrodes (120 nm) were used for Ohmic contacts. The chemical structure of the ZTO films modified by the O₃ treatment was evaluated by Fourier transformed infrared (FTIR, Nicolet 6700, Thermo Scientific, USA) spectroscopy in absorption mode. The thick ZTO films (550 nm) for FTIR analysis were prepared by sputter deposition on a bare Si wafer. The surface wettability of the films was examined by measuring the contact angle of water droplets on the surface of the ZTO films using a Phoenix 300 contact angle analyzer (Surface Electro Optics, Korea).

3.5 Electrical and Reliability Measurements

The electrical and Reliability characteristics were measured using HP 4145B and HP 4155A semiconductor parameter analyser at room temperature in air ambient. The V_{th} was determined by adjusting the gate voltage, which induces a drain current of $L/W \times 10$ nA at $V_{DS} = 10$ V.³¹ To characterize the effects of negative bias illumination stress (NBIS) on the transfer characteristics of the ZTO-based FETs, the devices were stressed under the following conditions: a constant voltage (- 20 V) stress was applied to the gate of transistor, while the applied drain voltage was 10 V at room temperature, respectively, and the maximum stress duration was 3,000 s ~ 5000 s. The transfer curves were taken from one device, which means that the applied NBIS was interrupted in order to measure each IV curve as a function of the applied NBIS time. A white halogen lamp was employed as a light source and the photon wavelength was approximately 650 nm, which was selected through band-pass filters. The photo-intensity was 0.1 ~ 0.5 mW/cm², as calibrated by photometry. The schematics of the illumination system were shown in Fig. 3.5.1.

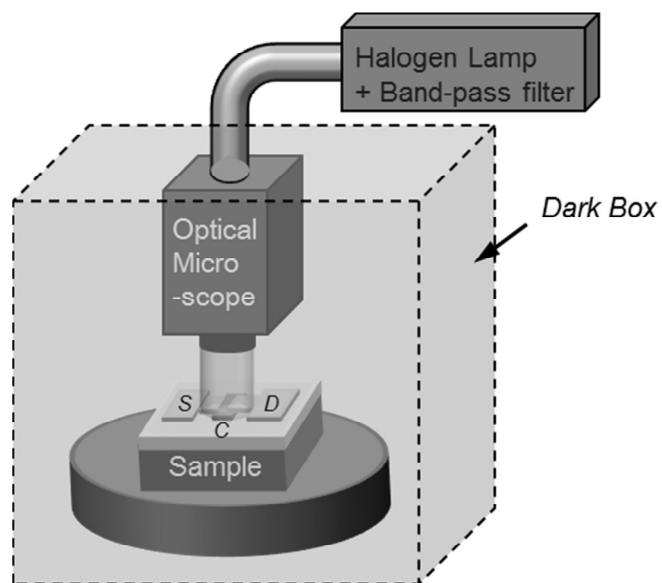


Fig. 3.5.1. Schematic diagram of the illumination system.

Chapter 4. The effect of bias illumination stress on the TFT reliability

4.1 Role of ZrO₂ incorporation in the suppression of negative bias illumination-induced instability in Zn-Sn-O thin film transistors

4.1.1 Introduction

Metal oxide field-effect transistors have strong potential to be used in emerging switching devices, including as thin film transistor (TFT) backplanes for high-end liquid crystal displays (LCDs), transparent organic light emitting diodes (OLEDs) and flexible displays, because they provide superior properties to those of amorphous Si (a-Si) semiconductor and polycrystalline Si TFTs, including a high mobility of $> 10 \text{ cm}^2/\text{V s}$, excellent uniformity, and good transparency to visible light.³³ The bias-thermal instability (BTI) of metal oxide TFTs is one of the critical issues remaining to be resolved before their implementation in commercial electronic products.³⁶⁻³⁸ The degradation mechanism of positive BTI (PBTI) for metal oxide TFTs has been intensively studied and can be attributed to the trapping of electron carriers accumulated in the channel layer,³⁶ the creation of defects in the semiconductor,³⁷ and/or the ambient dynamics of the un-

encapsulated back channel region.³⁸ Based on this assignment, the improvement of the PBTI has been achieved by optimizing the gate dielectric and passivation layer.^{31,39,40} In contrast, less attention was paid to the negative BTI (NBTI) until it was reported that the performance degradation associated with the threshold voltage (V_{th}) is more severe for NBTI than for PBTI under simultaneous light stress.⁴¹ Because the operation of active matrix LCDs and transparent displays inevitably suffers from light induced stress, including that resulting from the back light unit and/or external visible light, the negative bias illumination stress (NBIS)-induced instability of metal oxide TFTs is still one of the crucial obstacles to their practical application. In this regard, intensive efforts have been made to understand the origin of this NBIS instability.^{42,48,55-58} Three degradation models have been proposed which can be considered as plausible origins: the trapping of photo-generated hole carriers,^{42,48,55} the creation of ionized oxygen vacancy defects,^{56,57} and the photo-desorption of oxygen-related molecules.⁵⁸ So far, the most studied systems were In-Ga-Zn-O^{42,55-57} and Hf-In-Zn-O⁴⁸ channel materials. However, the In is a rare earth element so these systems suffer from the problems of scarcity in the crust of the earth as well as expensive material costs.

In this study, the use of Zn-Sn-O (ZTO) material as an In and Ga-free multi-component system and the effect of ZrO₂ incorporation on the negative and positive bias illumination stress instability of the resulting Zn-

Sn-Zr-O (ZTZO) TFTs are reported. It was found that the incorporation of ZrO_2 into the ZTO films increased the contact resistance, which led to the degradation of the transport properties of ZTZO TFTs. However, the ZrO_2 doping via co-sputtering into the ZTO film strongly suppresses the BIS instability of the resulting ZTZO TFTs. This improvement was attributed to the reduction in the concentration of oxygen vacancies as a result of the doping of ZrO_2 . In addition, from the bulk XPS results, the surface condition of ZTO films is an important factor determining the photo-bias stability of metal oxide FETs.

4.1.2 Experiment

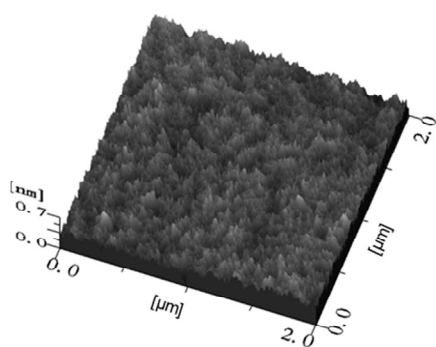
36-nm-thick ZTO and ZTZO channel layers were deposited by reactive RF magnetron sputtering on highly doped p-type silicon wafers with a 100-nm-thick thermal oxide layer. A high quality thermal SiO₂ film was used as a gate insulator, in order to prevent the injection of charge carriers into the underlying gate dielectric under bias illumination stress conditions.⁴² A 3-inch diameter ZnO:SnO₂ ceramic target and ZrO₂ target were utilized as the ZTO and ZrO₂ precursors, respectively, with a substrate-to-target distance of ~ 15 cm. During channel deposition, the rf power of the ZTO target was fixed at 100W, while that of the ZrO₂ target was varied. The chamber pressure was 5 mTorr and the oxygen to Ar (O₂/Ar) gas ratio was 0.3. Then, a 100-nm-thick source/drain electrode composed of tin-doped indium oxide (In₂O₃ : SnO₂ = 90 : 10 wt %) was formed by the dc sputtering process at room temperature. The channel and source/drain electrodes were patterned using a shadow mask with a channel length of 300 μm and a width of 1000 μm. After the deposition, the samples were annealed in a vertical type quartz tube furnace at a temperature of 350 °C for 1 hour in air ambient. The electrical characteristics of the TFTs were measured at room temperature with an HP 4155A semiconductor parameter analyser (SPA). Standard Θ -2 Θ X-ray diffraction (XRD, X'Pert-PRO, PANalytical) measurements were performed using Cu K_α radiation to evaluate the

crystallinity. High-resolution X-ray reflectivity (XRR) measurements were performed to determine the roughness, density, and thickness of the ZTO and ZTZO thin films. The XRR data so obtained were fitted using the PANalytical X'Pert Reflectivity software package. The surface wettability of the films was examined by measuring the contact angle of water droplets on the surface of the ZTO films using a Phoenix 300 contact angle analyzer (Surface Electro Optics, Korea). Hall effect measurements for the ZTO and ZTZO films were carried out using the van der Pauw configuration. The thermal evaporated aluminium electrodes (120 nm) were used for Ohmic contacts.

4.1.3 Results and Discussions

Figures 4.1.1(a) and 4.1.1(b) depict the surface morphology, obtained by atomic force microscopy, for the ZTO and $\text{Zn}_{0.54}\text{Sn}_{0.42}\text{Zr}_{0.04}\text{O}$ films, respectively. The root-mean-square (rms) roughness for the ZTZO film was not affected by the incorporation of ZrO_2 : Both films exhibited the same rms roughness of ~ 0.8 nm. The crystallographic structure of the ZTO film was also independent of the ZrO_2 incorporation, as shown in Fig. 4.1.2. Both films were amorphous. Figure 4.1.3 shows the XRR data for both films. The best fitting result is summarized in Table 4.1.1. The film densities obtained from the XRR simulation result were 5.05 and 5.40 g/cm^3 for the ZTO and ZTZO films, respectively. The incorporation of Zr with only $\sim 4\%$ concentrations may not explain such large increase in density. Higher density of ZTZO film than ZTO film is thought to be related to the ion bombardment effect by additional ZrO_2 plasma power. The thicknesses of both films were the same (~ 36 nm), but the XRR-derived roughness of the ZTZO film was slightly larger than that of the ZTO film. The electron concentration (N_d) of the ZTZO films decreased with increasing ZrO_2 incorporation. The N_d of the $\text{Zn}_{0.54}\text{Sn}_{0.42}\text{Zr}_{0.04}\text{O}$ films was reduced from $6.1 \pm 0.8 \times 10^{17} \text{ cm}^{-3}$ (ZTO film) to $2.4 \pm 0.5 \times 10^{16} \text{ cm}^{-3}$.

(a) $R_{\text{rms}} : 0.8 \text{ nm}$



(b) $R_{\text{rms}} : 0.8 \text{ nm}$

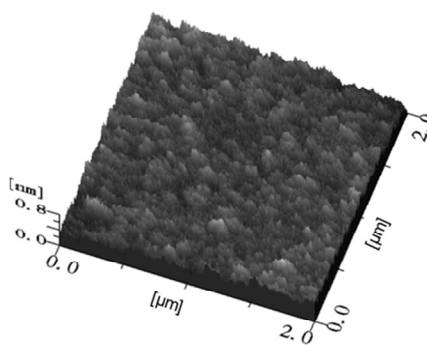


Fig. 4.1.1. AFM images ($2 \mu\text{m} \times 2 \mu\text{m}$) of post-annealed (a) ZTO and (b) $\text{Zn}_{0.54}\text{Sn}_{0.42}\text{Zr}_{0.04}\text{O}$ thin films.

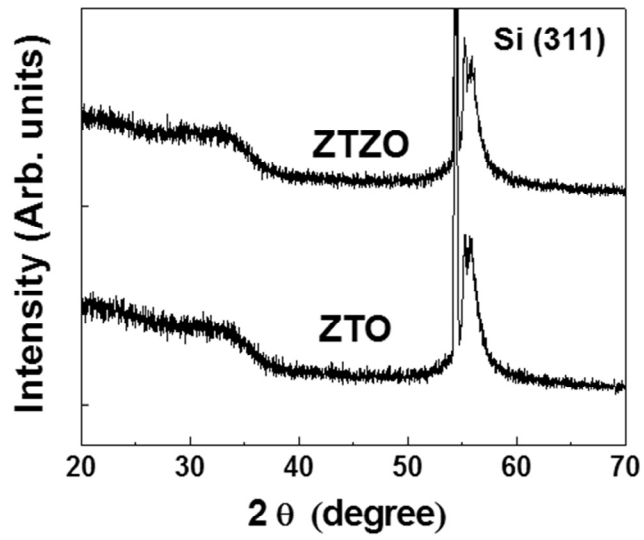


Fig. 4.1.2. X-ray diffraction patterns of the post-annealed ZTO and $\text{Zn}_{0.54}\text{Sn}_{0.42}\text{Zr}_{0.04}\text{O}$ thin films.

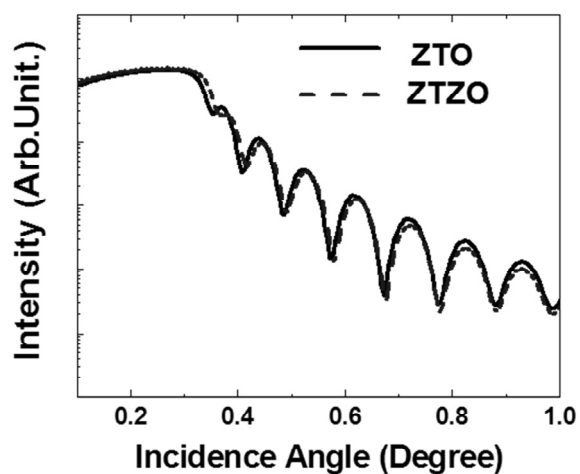


Fig. 4.1.3. The X-ray reflectivity spectrum for the post-annealed ZTO (line) and $\text{Zn}_{0.54}\text{Sn}_{0.42}\text{Zr}_{0.04}\text{O}$ (dashed) thin films.

Table 4.1.1. Best-simulated XRR results for ZTO and $\text{Zn}_{0.54}\text{Sn}_{0.42}\text{Zr}_{0.04}\text{O}$ thin films of Fig. 4.1.3.

Layer	Density (g/cm^3)	Thickness (nm)	R_{rms} (nm)
ZTO	5.05	36.2	1.371
$\text{Zn}_{0.54}\text{Sn}_{0.42}\text{Zr}_{0.04}\text{O}$	5.40	36.3	1.682

Figures 4.1.4(a) and 4.1.4(b) show the transfer characteristics for the ZTO TFT and $Zn_{0.54}Sn_{0.42}Zr_{0.04}O$ TFT, respectively. The V_{GS} was swept from -20 V to 20 V. Figure 4.1.5 shows the change in the transfer curve of ZTO and $Zn_{0.54}Sn_{0.42}Zr_{0.04}O$ TFTs under negative bias stress in dark (NBS) and with illumination (NBIS). Figure 4.1.8 shows the evolution of the transfer curve for the ZTO and $Zn_{0.54}Sn_{0.42}Zr_{0.04}O$ TFTs as a function of the applied positive bias stress in dark (PBS) and with illumination (PBIS). The pristine device characteristics correspond to the transfer curves measured at 0 s (before stress). V_{th} was defined as the gate voltage which induces a drain current of $L/W \times 10$ nA at $V_{DS} = 10.1$ V.³¹ The field-effect mobility (μ_{FE}) was determined from the slope of the plot of I_{DS} vs. V_{GS} in the linear region according to the following expression: $I_{DS} = (WC_i/L)\mu_{FE}(V_{GS} - V_{th})V_{DS}$ where L is the channel length, W is the width, and C_i is the gate capacitance per unit area. The subthreshold gate swing ($SS = dV_{GS}/d\log I_{DS}$ [V/decade]) was extracted from the linear part of the plot of $\log(I_{DS})$ vs. V_{GS} . The ZTO TFT exhibited μ_{FE} , V_{th} , SS and $I_{on/off}$ ratio values of 19.1 cm^2/Vs , -0.55 V, 0.45 V/decade and 1.2×10^8 , respectively. A slight degradation of the device performance was observed for the TFTs with the $Zn_{0.54}Sn_{0.42}Zr_{0.04}O$ channel layer. The $Zn_{0.54}Sn_{0.42}Zr_{0.04}O$ TFT had a μ_{FE} of 8.9 cm^2/Vs , V_{th} of 0.7 V, SS of 0.7 V/decade and $I_{on/off}$ ratio of 7.5×10^8 before the NBIS test. The diminishing μ_{FE} and increasing V_{th} value for the ZTZO TFTs with increasing Zr content can be understood by conducting an analysis using the transfer

line method (TLM).²⁹ Figure 4.1.10 shows the results of the TLM measurement. In fig. 4.1.10(c), total resistances (R_T) of ZTO film were extracted from the slop of the I-V characteristics. Figure 4.1.10(d) shows width-normalized contact resistances (R_{CW}) for the ZTZO TFTs with various ZrO_2 contents, which were extracted by the TLM. As the ZrO_2 content increased, the R_{CW} value of the TFTs increased from 190.9 Ωcm for the ZTO only device to 1474.3 Ωcm for the device with the $Zn_{0.54}Sn_{0.42}Zr_{0.04}O$ channel. Therefore, the deteriorated performance for the ZTZO TFTs is attributed to the reduced carrier density of the ZTZO channel layer.³³

Next, the NBIS and PBIS instabilities for both devices were examined. Figure 4.1.5 show the evolution of the transfer characteristics as a function of the NBS time (Figs. 4.1.5(a) and (b)) and NBIS time (Figs. 4.1.5(c) and (d)). Figures 4.1.6 (a) and (b) shows the variance of V_{th} in the TFTs under Dark-NBS and NBIS conditions. The devices were stressed under the following conditions: a constant voltage (- 20 V) stress was applied to the gate of transistor, while the applied drain voltage was 10 V at room temperature, respectively. The TFTs were illuminated ($\lambda=650$ nm, 0.1 mW/cm^2) by a halogen lamp through band-pass filters for NBIS measurement. The NBIS was applied for 5,000 s in air ambient. In Figs. 4.1.5(a) and (b), it can be shown that the dark stability without light illumination under the same negative bias stress (NBS) conditions was much

better than those induced by NBIS: the ZTO and $\text{Zn}_{0.54}\text{Sn}_{0.42}\text{Zr}_{0.04}\text{O}$ devices suffered from negative shifts of V_{th} of only 2.8 V and 0.8 V, respectively, after the application of dark NBS for 5,000 s. This small negative V_{th} shift under the dark NBS condition can be attributed to either the hole carrier trapping at existing defect^{59,60} or the dynamical interaction of ambient such as oxygen or/and moisture.⁶¹ On the other hand, a huge negative V_{th} shift of 12.5 V for the ZTO device with increasing NBIS time occurred without an accompanying change in μ_{FE} and the $I_{\text{on/off}}$ ratio (Figs. 4.1.5(c) and 4.1.6(b)). This negative V_{th} displacement was significantly diminished to be $\sim 4.2\text{V}$ for the $\text{Zn}_{0.54}\text{Sn}_{0.42}\text{Zr}_{0.04}\text{O}$ device [see Figs. 4.1.5(d) and 4.1.6(b)]. It was proposed that the photo-enhanced negative V_{th} shift under NBS conditions comes from the photo-transition of the oxygen vacancies from V_{O} to V_{O}^{2+} in the oxide semiconductor.^{56,57} In this model, the thermodynamically stable V_{O} state is assumed to be excited to the meta-stable V_{O}^{2+} state by photon irradiation, leading to two delocalized free electrons in the conduction band of the oxide semiconductor.⁶²⁻⁶⁴ The accumulation of V_{O}^{2+} due to its diffusion toward the channel/gate insulator interface by the applied negative gate bias under NBIS conditions may cause the negative V_{th} shift. Figure 4.1.7 shows the SS variation for the ZTO and ZTZO devices under the (a) dark NBS and (b) NBIS condition, respectively. Interestingly, the application of NBIS simultaneously caused the increase in SS values (equivalently increasing trap states) of both devices while the SS values for both devices

were not changed under the dark NBS condition, suggesting that this NBIS-created trap states would be related to the metastable Vo^{2+} defects.

Figure 4.1.8 show the change in the transfer curve for different of the PBS time (Figs. 4.1.8(a) and (b)) and PBIS time (Figs. 4.1.8(c) and (d)). Figures 4.1.9 (a) and (b) shows the variance of V_{th} in the TFTs under Dark-PBS and PBIS conditions. A constant positive voltage (+ 20 V) stress was applied to the gate of transistor, while the applied drain voltage was 10 V at room temperature, respectively. The devices were stressed under the same illumination conditions with NBIS measurement. As shown in Figs. 4.1.8, the dark stability without light illumination under the same positive bias stress (PBS) conditions was better than those induced by PBIS. The ZTO device suffered from positive V_{th} shifts of 4.44 V after the application of dark PBS for 5,000 s. In contrast, the $\text{Zn}_{0.54}\text{Sn}_{0.42}\text{Zr}_{0.04}\text{O}$ device exhibited a decrease 3.05 V in V_{th} under the same PBS conditions. A positive V_{th} shift of 4.90 V for the ZTO device with increasing PBIS time occurred without an accompanying change in μ_{FE} and the $I_{\text{on/off}}$ ratio. This negative V_{th} change was diminished to be 3.63 V for the $\text{Zn}_{0.54}\text{Sn}_{0.42}\text{Zr}_{0.04}\text{O}$ device under the PBIS conditions. The state creation during bias stress measurement is accompanied by change in the S.S value and mobility, but there is no change in the case of charge trapping.⁶⁵ Therefore, this positive V_{th} shift under the PBS condition can be attributed to the charge trapping at the insulator

and/or interface, or the dynamical interaction of ambient such as oxygen or/and moisture.⁶¹ In addition, oxygen vacancies may act as trap states.⁶⁶

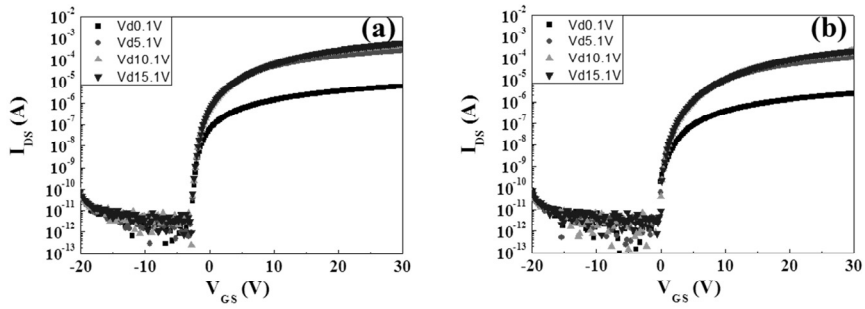


Fig. 4.1.4. Representative transfer characteristics of TFTs with (a) ZTO and (b) $\text{Zn}_{0.54}\text{Sn}_{0.42}\text{Zr}_{0.04}\text{O}$ channel layers.

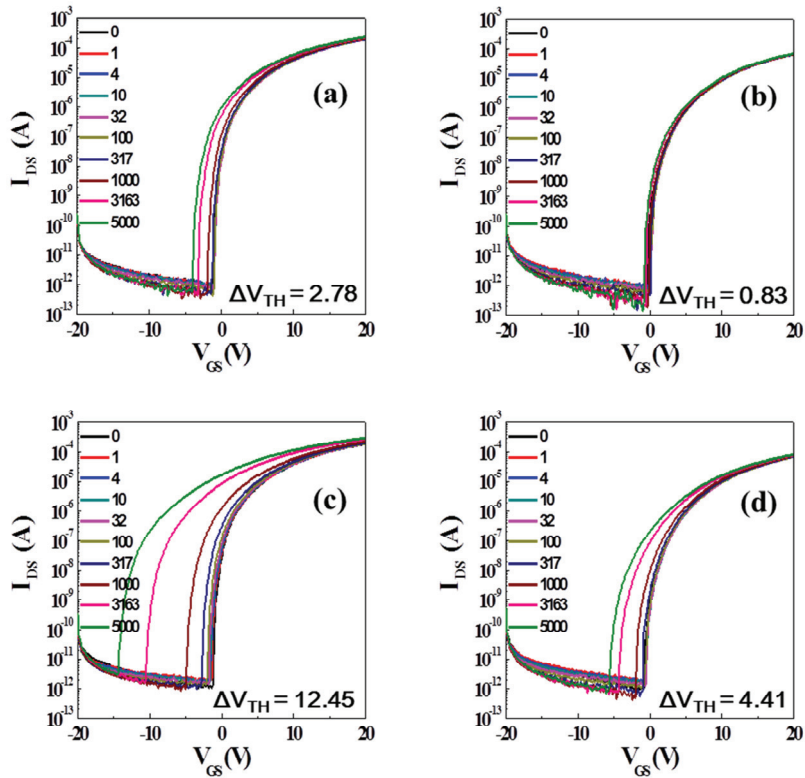


Fig. 4.1.5. Variations of the transfer characteristics as a function of the applied stress time with ZTO and $Zn_{0.54}Sn_{0.42}Zr_{0.04}O$ (ZTZO) channel layers; (a) NBS of ZTO, (b) NBS of ZTZO, (c) NBIS of ZTO, (d) NNBS of ZTZO.

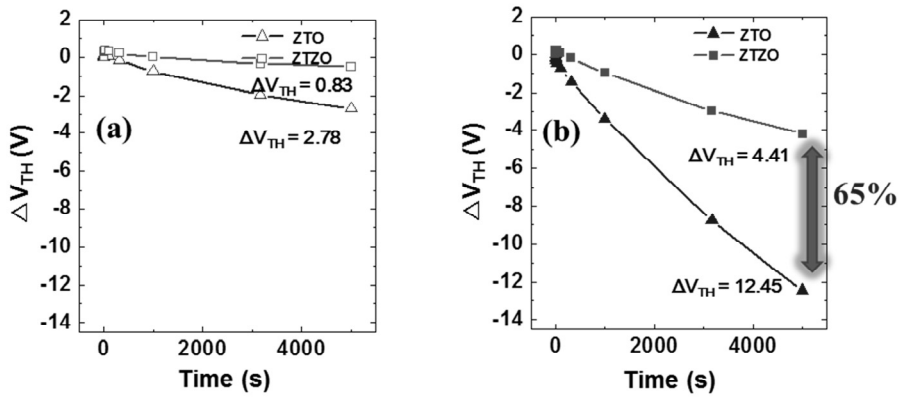


Fig. 4.1.6. Variations in V_{th} value as a function of the applied stress time for ZTO and $Zn_{0.54}Sn_{0.42}Zr_{0.04}O$ TFTs; (a) Dark-NBS condition, (b) NBIS condition.

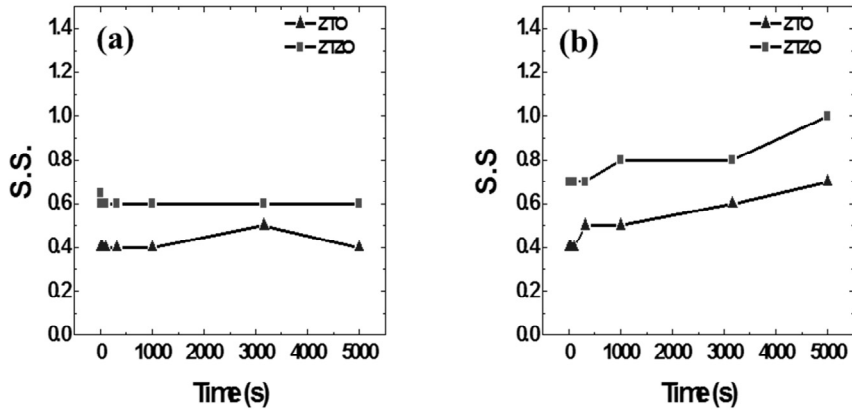


Fig. 4.1.7. Comparison of the SS variations for the ZTO and ZTZO devices under the (a) Dark- NBS condition, (b) NBIS condition.

Table 4.1.2. Device characteristics and Variations in V_{th} value for the ZTO and $Zn_{0.54}Sn_{0.42}Zr_{0.04}O$ FETs.

Sample	V_{TH} (V)	S.S (V/dec.)	μ_{SAT} (cm^2/Vs)	μ_{SAT} (cm^2/Vs)	NBS ΔV_{TH} (V)	NBIS ΔV_{TH} (V)
ZTO	-0.55	0.45 (± 0.05)	19.1	11.2	2.78	12.45
ZTZO	0.69	0.7 (± 0.05)	8.9	4.8	0.83	4.41

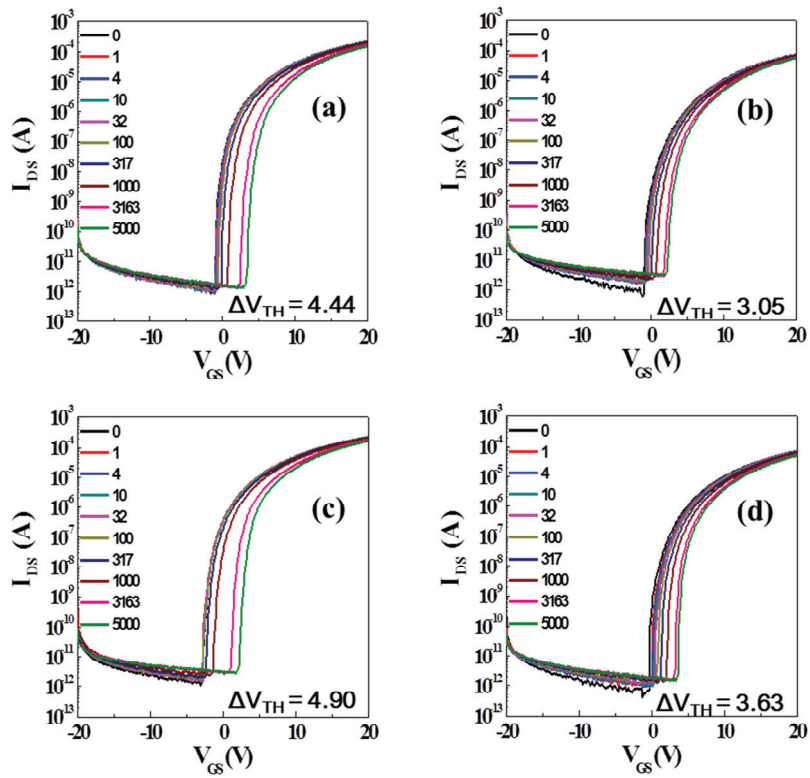


Fig. 4.1.8. Variations of the transfer characteristics as a function of the applied stress time with ZTO and $Zn_{0.54}Sn_{0.42}Zr_{0.04}O$ (ZTZO) channel layers; (a) PBS of ZTO, (b) PBS of ZTZO, (c) PBIS of ZTO, (d) PNBIS of ZTZO.

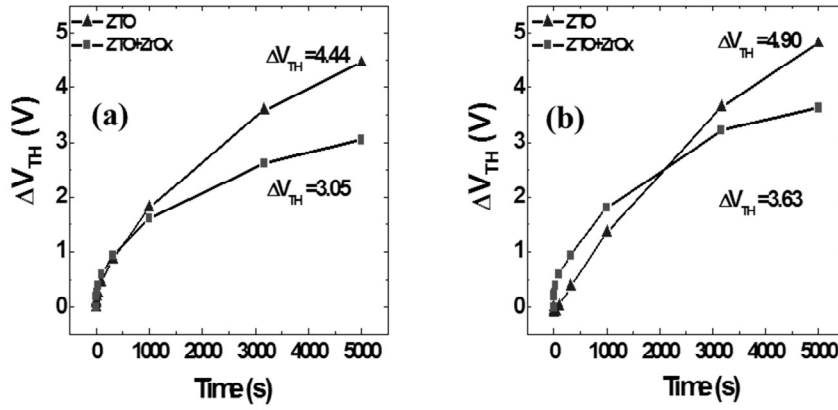


Fig. 4.1.9. Variations in V_{th} value as a function of the applied stress time for ZTO and $Zn_{0.54}Sn_{0.42}Zr_{0.04}O$ TFTs; (a) Dark-PBS condition, (b) PBIS condition.

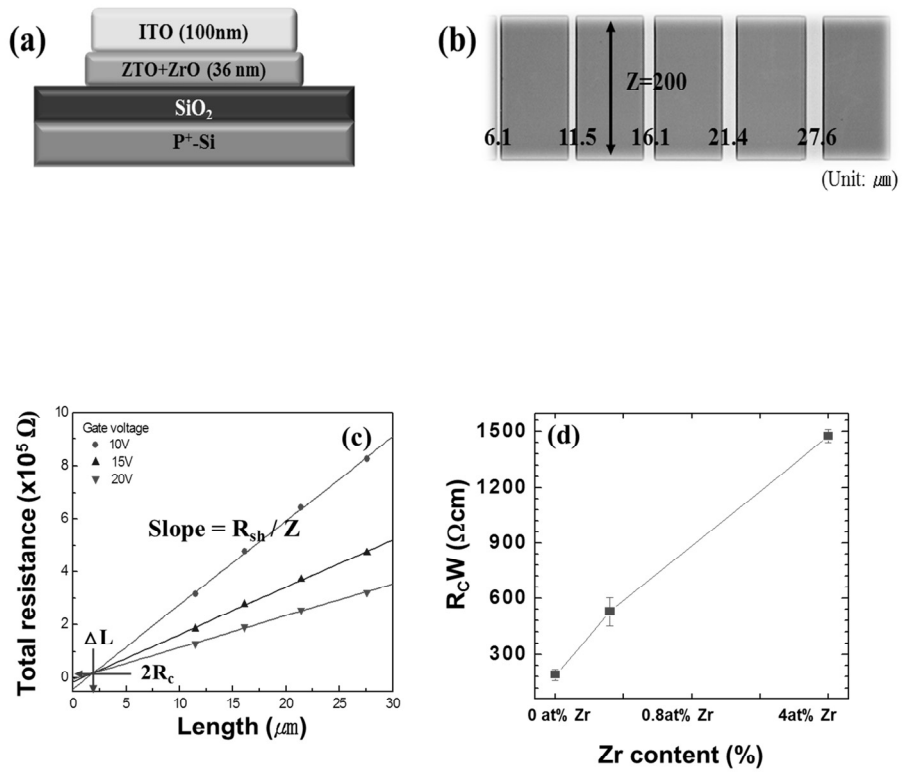


Fig. 4.1.10. The results of TLM measurements; (a) the device structure, (b) the design of TLM patterns. (c) Gate voltage dependence of the total resistance Variations of ZTO film. (d) The width-normalized R_c variation in the fabricated TFTs as a function of the Zr content.

In order to verify this model, the chemical state of oxygen in the ZTO and ZTZO thin films was investigated. Figure 4.1.11 shows their O *1s* XPS spectra after thermal annealing at 350 °C. To calibrate the photoelectron binding energy, the C *1s* peak attributed to C-C bonds was set to 284.5 eV. The O *1s* spectra were de-convoluted into three different peaks, which are assigned as follows: the “lattice oxygen peak without oxygen vacancies” (530.0 eV), the “lattice oxygen peak in the oxygen-deficient region” (531.1 eV), and a metal hydroxide peak” (531.9 eV).⁶⁷ It can be clearly seen that the relative area of the oxygen vacancy-related peak at 531.1 eV decreased with increasing ZrO₂ fraction in the ZTZO film. The values are 29.8%, 24.0%, and 20.2% for the ZTO, Zn_{0.57}Sn_{0.42}Zr_{0.008}O and Zn_{0.54}Sn_{0.42}Zr_{0.04}O films, respectively. The decreasing proportion of the peak area corresponding to oxygen vacancies with increasing ZrO₂ content strongly indicates that the improvement of the photo-stability for the higher content ZrO₂ devices under NBS and PBS conditions arose from the reduction of the V_O defect density. Diminishing the [V_O] portion by ZrO₂ incorporation is thought to be related to the fact that the Gibbs free energies of formation (ΔG_f) for ZnO, SnO, SnO₂ and ZrO₂ are -320.4, -256.7, -520.0 and -1039.7 kJ/mole, respectively, in their standard states.⁶⁸ The most negative ΔG_f value (-1039.7 kJ/mole) of ZrO₂ suggests that the chemical bonding with respect to oxygen atoms is the strongest among the Zn, Sn and Zr cation atoms. Thus, increasing the Zr content in the ZTO system will decrease the concentration of V_O. It should

be emphasized that the reducing creation probability of V_O defects by incorporating agency such as ZrO_2 can improve the photo-stability of the resulting ZTZO TFTs under NBS and PBS conditions, although it is also accompanied by diminished conduction properties (lower mobility and increasing V_{th}) as a result of the increase in R_C . Therefore, the photo-transition model of V_O for NBS and electron trapping model by oxygen vacancy for PBS are consistent with the XPS results.

The profiling of O $1s$ XPS spectra after etching the surface was carried out in order to evaluate the reduction of V_O defect density in bulk region. Figure 4.1.12 shows the evolution of de-convoluted O $1s$ XPS spectra for the ZTO and ZTZO films in bulk region after etching the surface. In the case of the ZTO film, the relative $[V_O]$ peak portion was diminished from 29.8% (surface) to 10.6% at the bulk region, as summarized in Table 4.1.2. In contrast, the $[V_O]$ portion for the $Zn_{0.54}Sn_{0.42}Zr_{0.04}O$ film was rapidly reduced from 20.2% (surface) to 6.2% at the bulk region. This result confirms that the ZrO_2 incorporation can effectively annihilate the V_O defects in the bulk region as well as the film surface. It is evident that the surface region of ZTO film suffered from the high $[V_O]$ concentration compared to the bulk region of ZTO film. In addition, it should be noted that the relative area of the metal hydroxide peak at 531.9 eV was increased with increasing ZrO_2 incorporation in the ZTZO films, suggesting that the OH-impurities from the ambient atmosphere may be preferentially adsorbed on

the ZrO_2 surface. The OH- impurities incensement was reconfirmed further by investigating the water wetting properties of ZTO and ZTZO films. Figure 4.1.13 shows the change in the water contact angle (WCA) as a function of Zr concentration in ZTO films. Although the WCA of the ZTO films was 39.4° , the $\text{Zn}_{0.54}\text{Sn}_{0.42}\text{Zr}_{0.04}\text{O}$ film showed a WCA of 22.7° , indicating that the Zr incorporation makes the film surface more hydrophilic. This is consistent with XPS results because the hydrophilicity of the ZTZO films is due to the higher number of polar groups, such as OH.⁶⁹ The photo-desorption mechanism can also be considered as a reason for the V_{th} shift under instability stress conditions.⁷⁰⁻⁷² The change in surface coverage with OH groups can affect the number of desorbed oxygen species on the ZTO surface during instability stress duration. This suggests that the surface region of ZTO films is an important factor determining the photo-bias stability of metal oxide TFTs. The depth study for surface effect on stability will be carried out in next chapter.

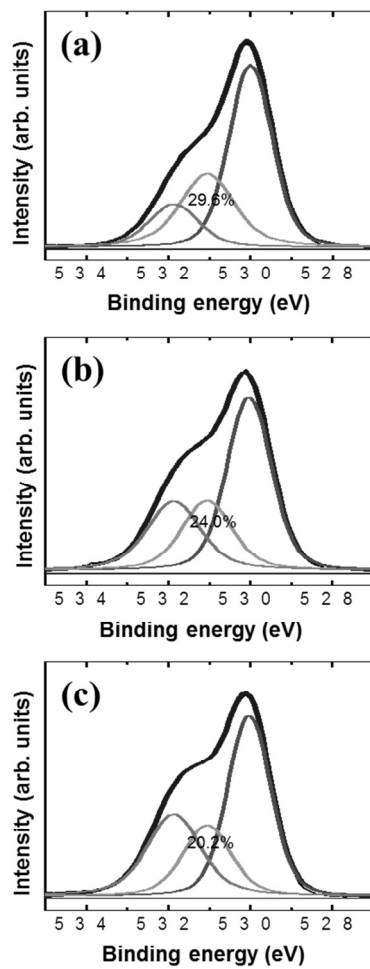


Fig. 4.1.11. XPS O 1s spectra and de-convolution results for the (a) ZTO, (b) $\text{Zn}_{0.57}\text{Sn}_{0.42}\text{Zr}_{0.008}\text{O}$ and (c) $\text{Zn}_{0.54}\text{Sn}_{0.42}\text{Zr}_{0.04}\text{O}$ thin films.

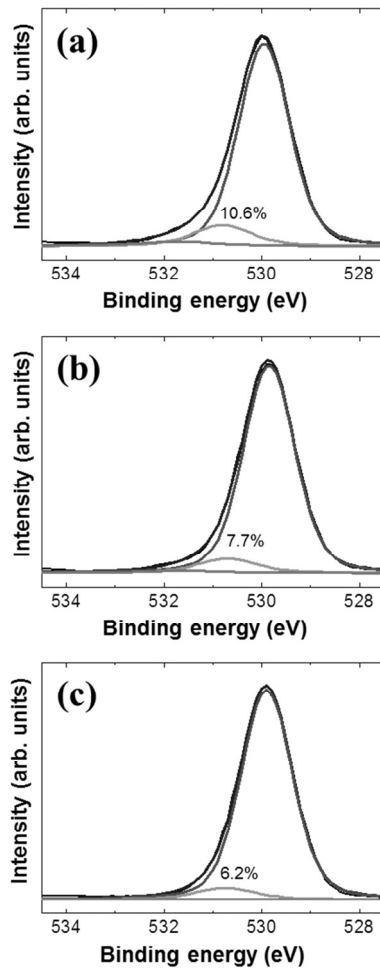


Fig. 4.1.12. XPS O $1s$ spectra and de-convolution results in bulk region for the (a) ZTO, (b) $\text{Zn}_{0.57}\text{Sn}_{0.42}\text{Zr}_{0.008}\text{O}$ and (c) $\text{Zn}_{0.54}\text{Sn}_{0.42}\text{Zr}_{0.04}\text{O}$ thin films.

Table 4.1.3. Comparison of portion of the O *1s* peaks deconvoluted from the XPS spectra at the surface of the ZTO-based films.

Samples	O <i>1s</i> peak [eV]		
	Lattice Oxygen (530.20 ± 0.04)	Oxygen deficient (531.06)	Hydroxyl (531.89)
ZTO	0.885	0.098	0.017
Zn _{0.57} Sn _{0.42} Zr _{0.008} O	0.887	0.099	0.013
Zn _{0.54} Sn _{0.42} Zr _{0.04} O	0.901	0.077	0.021

Table 4.1.4. Comparison of portion of the O *1s* peaks deconvoluted from the XPS spectra in the bulk of the ZTO-based films.

Samples	O <i>1s</i> peak [eV]		
	Lattice Oxygen (530.20 ± 0.04)	Oxygen deficient (531.06)	Hydroxyl (531.89)
ZTO	0.885	0.098	0.017
Zn _{0.57} Sn _{0.42} Zr _{0.008} O	0.887	0.099	0.013
Zn _{0.54} Sn _{0.42} Zr _{0.04} O	0.901	0.077	0.021

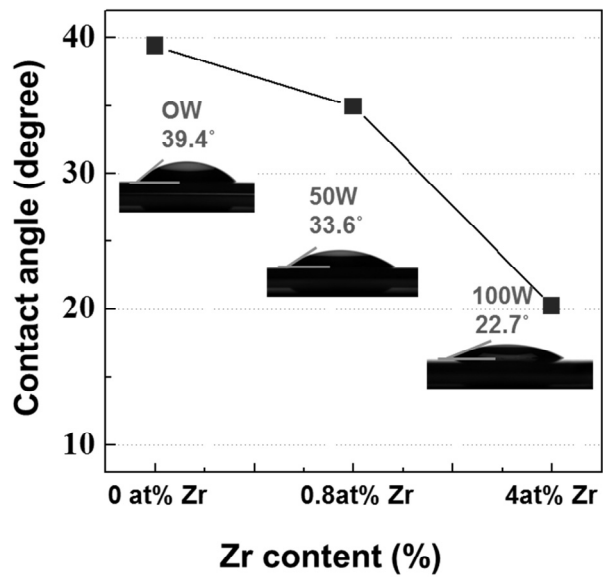


Fig. 4.1.13. Variations in contact angle of water droplets of ZTO films with different Zr doping ratio.

4.1.4 Summary

In summary, TFT with ZrO₂ incorporated ZTO channel layer was fabricated. And the effect of ZrO₂ incorporation in the ZTO film and field effect transistors (TFT) was investigated. As the ZrO₂ content increases, the μ_{FE} and V_{th} values were diminished and increased, respectively, which was attributed to the increase in R_C . However, in terms of the bias illumination stress instability, the Zr-incorporated ZTZO device exhibited much better photo-stability. While the ZTO device exhibited inferior V_{th} stability ($\Delta V_{th} = -12.5$ V) after the application of NBIS for 5,000 s, the stability ($\Delta V_{th} = -4.2$ V) of the ZTZO (ZrO₂ doped ZTO) device against NBIS was greatly improved, which was attributed to the reduction of the $[V_O]$ defect density in the ZTZO film. The relative area of the oxygen vacancy-related peak decreased with increasing ZrO₂ fraction in the ZTZO film. The decreasing proportion of the peak area corresponding to oxygen vacancies with increasing ZrO₂ content strongly indicates that the improvement of the photo-stability for the higher content ZrO₂ devices under negative and positive bias illumination stress conditions arose from the reduction of the V_O defect density. Therefore, the photo-transition model of V_O is consistent with the XPS results. This is thought to be related to the fact that the Gibbs free energies of formation (ΔG_f) for ZnO, SnO, SnO₂ and ZrO₂. The most negative ΔG_f value (-1039.7 kJ/mole) of ZrO₂ suggests that the chemical

bonding with respect to oxygen atoms is the strongest among the Zn, Sn and Zr cation atoms. Thus, increasing the Zr content in the ZTO system will decrease the density of V_O . From the bulk XPS, WCA results, it is evident that the surface region of ZTO film has a high $[V_O]$ and OH concentration compared to the bulk region of ZTO film. This suggests that the surface region of ZTO films is an important factor determining the photo-bias stability of ZTO-based TFTs.

As the result, the incorporation of an optimal amount of Zr into ZTO TFTs can provide a means to overcome the problem of NBIS instability, which would enable metal oxide TFTs to be used in AMLCDs, AMOLEDs and flexible/transparent electronics.

4.2 Improvement of the photo-bias stability of the Zn-Sn-O field effect transistors by an ozone treatment

4.2.1 Introduction

Recent advances in transparent oxide semiconductor materials have accelerated the development of field-effect transistors (FETs), which are the unit pixel driver for novel flexible display as well as active matrix flat panel displays (FPDs). The intriguing property of oxide FETs includes high mobility, good transparency and low processing capability compared to conventional amorphous Si FETs.^{32,33,73-75}

Although high performance oxide FETs can be fabricated in a straightforward manner through an examination of channel materials via the combinatorial approach, the device reliability against a gate bias stress or/and light stress still remains a critical issue for the implementation of oxide FETs to commercial electronic products. In-depth studies indicate that charge trapping at the defect states plays an important role in threshold voltage (V_{th}) instability under a gate bias or/and light stress condition.^{42-47,49,50,56,76,77} Considering that the n-type conductivity of ZnO-based semiconductors originates from oxygen-deficiencies, careful control of oxygen vacancies in the channel material is essential for improving the photo-bias stability of oxide FETs. In particular, the application of oxide

FETs to flexible displays requires low temperature processing (<200°C) because of the low softening temperature of bendable plastic substrates. The limitation of the process temperature involves the inevitable creation of point defect states, such as oxygen vacancies and metal cation interstitials etc., which cause further degradation of the device reliability. Therefore, a facile process to substantially reduce the point defect density in a metal oxide channel layer is of great importance, while maintaining the low thermal budget for the use of plastic substrates. The present study showed that highly stable zinc tin oxide (ZTO) FETs can be obtained by an ozone treatment at lower temperatures. As similar approaches, high pressure O₂ annealing and oxygen plasma treatments were demonstrated to reduce the oxygen deficiency concentration in oxide films.^{47,49} On the other hand, the present study showed that a simple oxygen vacancy reduction model cannot explain all the experimental observations, and suggested that the surface chemistry of ZTO films related to the chemical adsorption on the back surface of the channel plays a crucial role. In this study, the photo-bias stability of ZTO FETs was improved significantly by performing an ozone treatment, and the possible reasons for such highly stable behavior are also discussed in detail.

4.2.2 Experiment

The fabricated ZTO FETs have a bottom gate and top contact configuration. A highly-doped p-type silicon wafer itself was used as the gate electrode. A 100-nm-thick thermal oxide layer was grown as a gate dielectric. A 19-nm-thick ZTO channel layer was prepared by radio-frequency (rf) magnetron sputtering. A 3-inch diameter ZnO:SnO₂ ceramic target was placed approximately 15 cm from the substrate, and the input rf power of the ZTO target was fixed to 100W. The working pressure was 5 mTorr and the relative oxygen flow rate [O₂]/[Ar+O₂] was maintained at 0.3. The channel area was defined using a shadow mask during deposition of the ZTO film, and 100-nm-thick ITO source/drain (S/D) electrodes were deposited at room temperature using the same sputtering system. The channel width (W) and length (L) of the fabricated FETs were 1000 μm and 300 μm, respectively. Post-deposition-annealing (PDA) of ZTO films was performed in air ambient at 350 °C for 1 hour in a vertical-type quartz tube furnace. The ozone (O₃) treatment of ZTO films was conducted after post-deposition annealing (PDA) as follows: the chamber working pressure was kept at 5 torr; the O₃ treatment was performed at 210 °C and the treatment time was split into 0 s, 30 s, 300 s, and 600 s; and the O₃ flow rate was fixed to 50 g/min, which was generated from 400 sccm of O₂. The electrical characteristics were measured at room temperature in air using an HP 4155A

semiconductor parameter analyzer. The V_{th} was determined by adjusting the gate voltage, which induces a drain current of $L/W \times 10$ nA at $V_{DS} = 10$ V.³¹ The saturation mobility (μ_{sat}) was calculated from the slope of the $I_{DS}^{1/2}$ vs. V_{GS} plot according to the following expression: $I_{DS} = (WC_i/2L)\mu_{sat}(V_{GS} - V_{th})^2$, where L is the channel length, W is the width, and C_i is the gate capacitance per unit area. In addition, the subthreshold gate swing ($SS = dV_{GS}/d\log I_{DS}$ [V/decade]) was extracted from the linear part of the $\log(I_{DS})$ vs. V_{GS} plot. To characterize the effects of negative bias illumination stress (NBIS) on the transfer characteristics of the ZTO FETs, the devices were stressed under the following conditions: V_{GS} and V_{DS} were set to -20 V and 10 V at room temperature, respectively, and the maximum stress duration was 3,000 s. A white halogen lamp was employed as a light source and the photon wavelength was approximately 650 nm, which was selected through band-pass filters. The photo-intensity was ~ 0.5 mW/cm², as calibrated by photometry. The transfer curves were taken from one device, which means that the applied NBIS was interrupted in order to measure each IV curve as a function of the applied NBIS time.

The chemical structure of the ZTO films modified by the O₃ treatment was evaluated by X-ray photoelectron spectroscopy (XPS, SIGMA PROBE, ThermoVG, U.K) and Fourier transformed infrared (FTIR, Nicolet 6700, Thermo Scientific, USA) spectroscopy in absorption mode. The thick ZTO films (550 nm) for FTIR analysis were prepared by sputter deposition

on a bare Si wafer. The surface wettability of the films was examined by measuring the contact angle of water droplets on the surface of the ZTO films using a Phoenix 300 contact angle analyzer (Surface Electro Optics, Korea). Standard Θ -2 Θ X-ray diffraction (XRD, X'Pert-PRO, PANalytical) measurements were performed using Cu K_{α} radiation to evaluate the crystallinity. High-resolution X-ray reflectivity (XRR) measurements were performed to determine the roughness, density, and thickness of the ZTO and ZTZO thin films. The XRR data so obtained were fitted using the PANalytical X'Pert Reflectivity software package.

4.2.3 Results and Discussions

Figure 4.2.1 shows the transfer characteristics of the ZTO FETs for different O₃ treatment times. The V_{GS} was swept from -20 V to 20 V. Figure 4.2.2 shows the change in the transfer curve of the ZTO FETs for different O₃ treatment times under negative bias stress with illumination (NBIS). The pristine device characteristics correspond to the transfer curves measured at 0 s (before stress). The O₃ untreated ZTO FET showed reasonable device performance with a μ_{sat} of 13.7 cm²/Vs, V_{th} of -0.16 V, SS of 0.28 V/decade and I_{on/off} ratio of 1.4×10^9 . Upon the O₃ treatment, the V_{th} and I_{on/off} ratio for the ZTO FETs were improved, whereas the mobility had decreased slightly: the 600 s-treated device exhibited a μ_{sat} , V_{th}, SS and I_{on/off} ratio of 11.3 cm²/Vs, 0.69 V, 0.32 V/decade and 6.8×10^{10} , respectively. The carrier density of the ZTO channel decreases due to a reduction in the oxygen vacancy concentration during the O₃ treatment, which results in a positive displacement of the V_{th} value and suppression of the off-state current.

Figure 4.2.3(a) and (b) summarizes the variations in V_{th} under Dark-NBS and NBIS conditions up to 3,000 s of the untreated (PDA only) and O₃ treated ZTO TFTs. The untreated ZTO FETs suffered from a large negative parallel shift (V_{th} ~ 4.2 V) after applying NBIS for 3,000 s, as shown in Figs. 4.2.2(a) and 4.2.3(b). Only the V_{th} shifted severely, whereas μ_{sat} and SS variations were not significant, suggesting that charge trapping

rather than defect creation in the channel region is the dominant degradation mechanism. In contrast, the 30 s-treated device exhibited a substantial decrease in V_{th} and only 0.57 V was observed under the same NBIS conditions. As the O_3 treatment time increased, the photo-bias stability of the ZTO FETs was enhanced further, as shown in Figs. 4.2.2(c), (d) and Figs. 4.2.3(b). Therefore, the 600 s-treated device almost did not suffer from a negative V_{th} displacement ($\Delta V = 0.07$ V), which is a highly promising result. The reasons for such improvement are discussed.

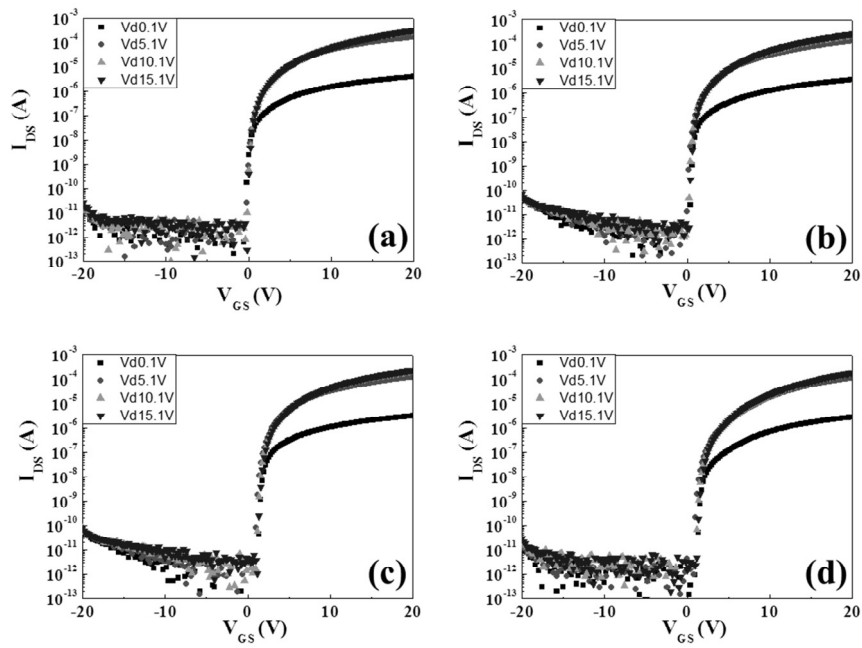


Fig. 4.2.1. Representative transfer characteristics of ZTO FETs with (a) untreated, (b) 30 s ozone treated, (c) 300 s ozone treated, and (d) 600 s ozone treated.

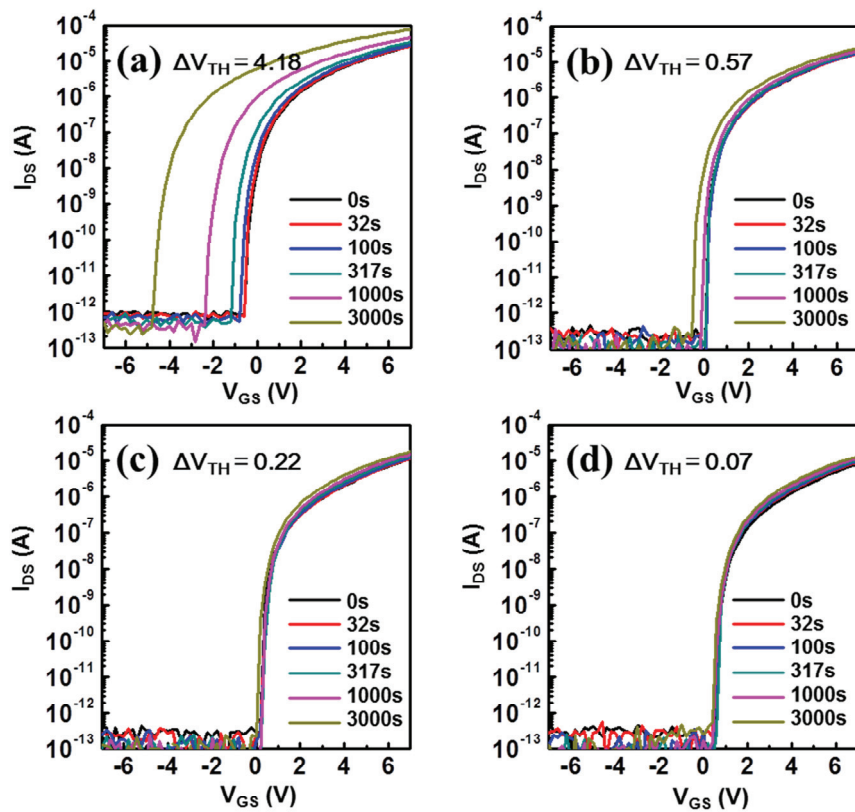


Fig. 4.2.2. Evolution of the transfer characteristics for (a) untreated, (b) 30 s ozone treated, (c) 300 s ozone treated, and (d) 600 s ozone treated ZTO FETs as a function of the NBIS time.

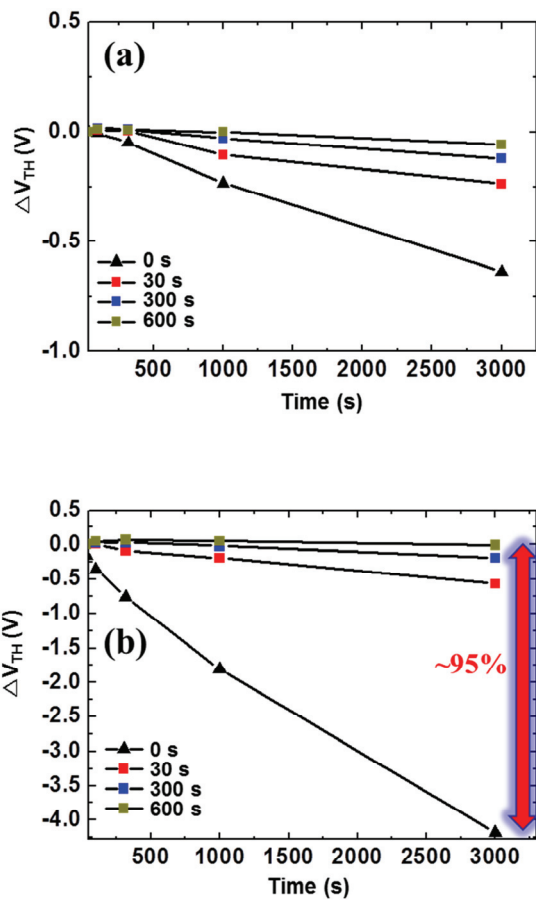


Fig. 4.2.3. Variations in V_{th} value as a function of the applied stress time for the different ZTO FETs; (a) Dark-NBS condition, (b) NBIS condition.

Table 4.2.1 Device characteristics and Variations in V_{th} value for the different ZTO FETs

Ozone Treatment time	V_{on} (V)	S.S (V/dec.)	μ_{SAT} (cm^2/Vs)	NBS ΔV_{TH} (V)	NBIS ΔV_{TH} (V)
PDA	-0.16	0.28	13.7	0.64	4.18
30 s	0.28	0.28	13.0	0.23	0.57
300 s	0.50	0.33	12.3	0.14	0.22
600 s	0.69	0.34	11.4	0.06	0.07

The negative V_{th} shift in the NBIS condition was attributed to i) the photo-induced hole trapping,⁴²⁻⁴⁵ ii) photo-transition⁴⁶ from V_O to V_O^{2+} [Here, the V_O and V_O^{2+} denote the oxygen vacancy with the neutral and +2 charge states, respectively.] and iii) photo-desorption of O_2 on the channel surface.⁴⁷ The hole trapping model assumes that photo-generated hole carriers are trapped at the gate dielectric/channel interfacial trap sites or gate dielectric bulk film.⁴³ Therefore, the hole trapping phenomena depends strongly on the gate dielectric material, which might be not responsible for the difference in the O_3 treatment-dependent V_{th} instability. A more plausible mechanism would involve the V_O concentration, $[V_O]$, in the ZTO film. Previously, it was reported that a V_O defect center acts as the source of hole carriers via V_O mediated e-h pair generation during NBIS.⁴⁹ Oxygen radicals will diffuse toward the bulk region of the ZTO film during the O_3 treatment. As a result, the O_3 treated device would have diminished pre-existing $[V_O]$, which may partially explain the improved NBIS stability.

The chemical state of oxygen in the ZTO film was examined to confirm the validity of this postulation. Figure 4.2.4 shows the XPS spectra of the O $1s$ of the untreated and O_3 treated ZTO films at the film surface. To calibrate the photoelectron binding energy, the C $1s$ peak for C-C bonds was assigned to 284.5 eV. The O $1s$ spectra were de-convoluted into three different peaks consisting of (i) a strong peak at a lower binding energy, which was assigned to the “lattice oxygen peak without oxygen vacancies”

(530.0 eV), (ii) a “lattice oxygen peak in the oxygen-deficient region” (531.1 eV), and (iii) a “metal hydroxide peak” (531.9 eV).⁷⁸ The relative intensities of three O *1s* peaks changed with the O₃ treatment time. Although the intensity of the lattice oxygen peak without oxygen vacancies was almost unchanged, the other two peaks were changed measurably with the O₃ treatment time. First, the relative area of the oxygen vacancy-related peak decreased monotonically with increasing O₃ treatment time. The values were 22.4%, 18.5%, 15.9%, and 13.1% for the untreated, 30 s, 300 s and 600 s O₃ treated ZTO films, respectively. This indicates that the O₃ treatment indeed reduces the [V_O] in ZTO films, supporting the oxygen vacancy model. Therefore, the decrease in [V_O] by the O₃ treatment is partially responsible for the improvement in NBIS stability of ZTO FETs.^{77,79} Second, the relative area of the metal hydroxide peak increased with increasing O₃ treatment time, suggesting that the surface coverage with hydroxyl bonding (OH) on the ZTO films had been increased substantially. The depth profiling of O *1s* XPS spectra was carried out in order to evaluate the reduction of [V_O] in bulk region as well. In the case of the untreated ZTO film, the relative [V_O] peak portion was diminished from 22.4% (surface) to 9.8% at the depth of ~ 4 nm (see Fig. 4.2.5, Fig. 4.2.6 and Table 4.2.3). It is evident that the surface region of ZTO film has a high [V_O] concentration compared to the bulk region of ZTO film. In contrast, the [V_O] portion for the 300 s ozone treated ZTO film was rapidly decreased from 15.9% (surface) to 7.7% at the depth

of ~ 4 nm as shown in Fig. 4.2.7 and Table 4.2.4. This result confirms that the ozone treatment can effectively annihilate the V_O defects in the bulk region (at least, up to ~ 4 nm from the surface) as well as the ZTO surface. It has been reported that the V_{th} shift under NBIS condition can be affected by the charge trapping of photo-generated hole carriers.^{43-45,49} The hole generated by photo-excitation moves to the channel/insulator interface by negative gate bias and injected into the insulator, which cause the negative V_{th} shift. A valence band offset between channel and insulator can affect the hole injection from channel layer to insulator. Figure 4.2.8 shows the valence band (VB) XPS of SiO_2 insulator (black line), untreated ZTO film, 30 s ozone treated, 300 s ozone treated, and 600 s ozone treated ZTO films. The reference level, 0 eV was taken from the Fermi level of the system. The VB offset between the ZTO and SiO_2 insulator was ~ 2.5 eV. However, the VB offset for the ozone treated ZTO film was not varied by the ozone treatment. Therefore, the V_{th} shift caused by NBIS was not induced by the difference of the charge trapping rate for the different ZTO FETs.

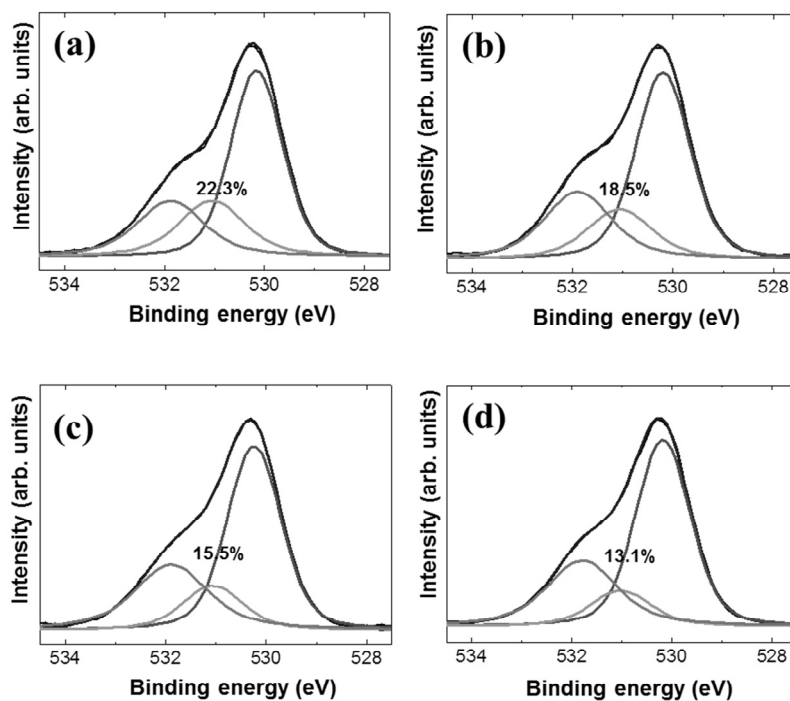


Fig. 4.2.4. XPS O 1s spectra, which were deconvoluted with three sub-peaks, of (a) untreated ZTO film, (b) 30 s ozone treated, (c) 300 s ozone treated, and (d) 600 s ozone treated ZTO films.

Table 4.2.2. Comparison of portion of the O 1s peaks deconvoluted from the XPS spectra at the surface of the ZTO-based films.

O₃ treatment time	O 1s peak [eV]		
	Lattice Oxygen (530.20 ± 0.04)	Oxygen deficient (531.06)	Hydroxyl (531.89)
0 s	0.549	0.224	0.227
30 s	0.552	0.185	0.262
300 s	0.551	0.159	0.289
600 s	0.581	0.131	0.288

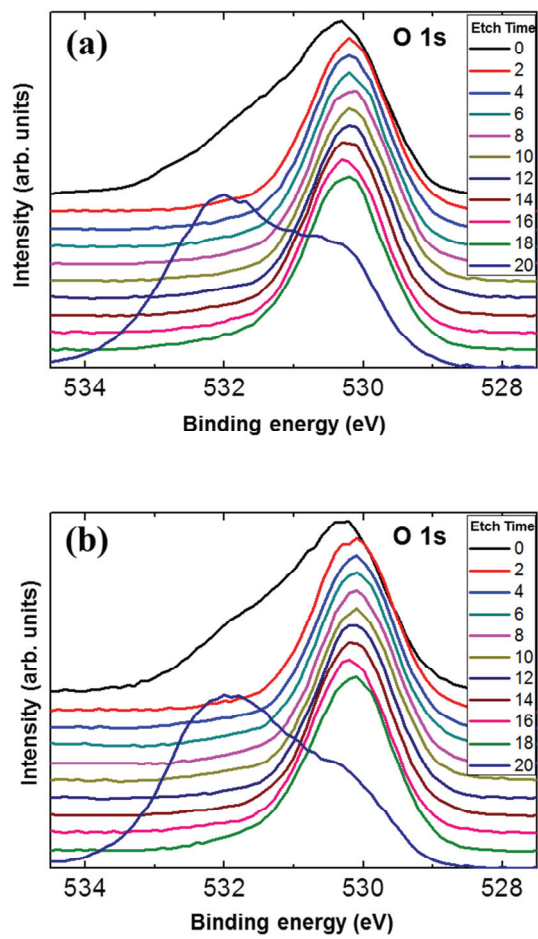


Fig. 4.2.5. Depth profiling of O 1s XPS spectra of (a) untreated and (b) 300 s ozone treated ZTO films.

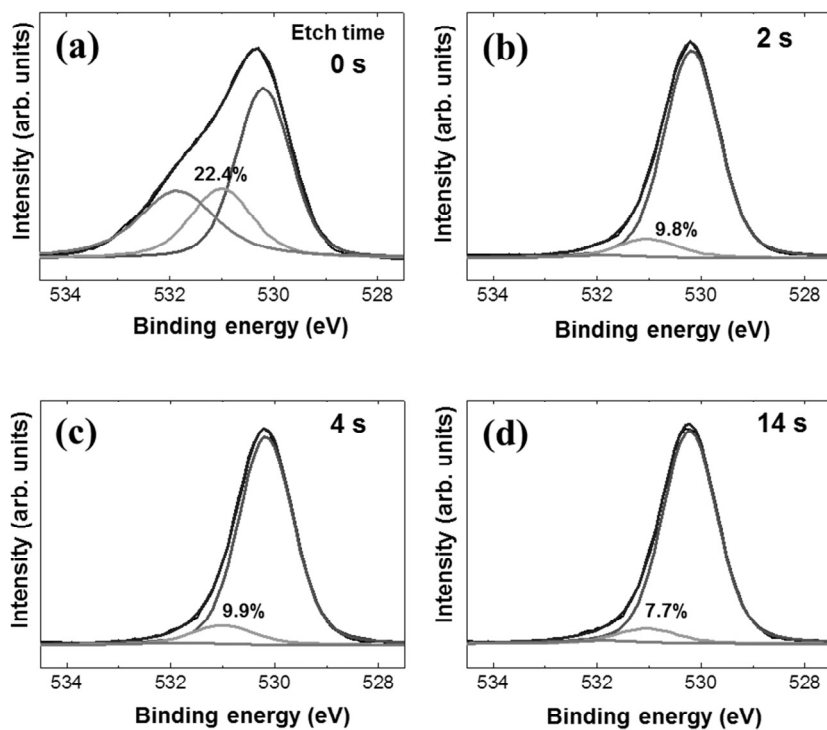


Fig. 4.2.6. The evolution of deconvoluted O 1s XPS spectra of the untreated ZTO films as a function of XPS etch time.

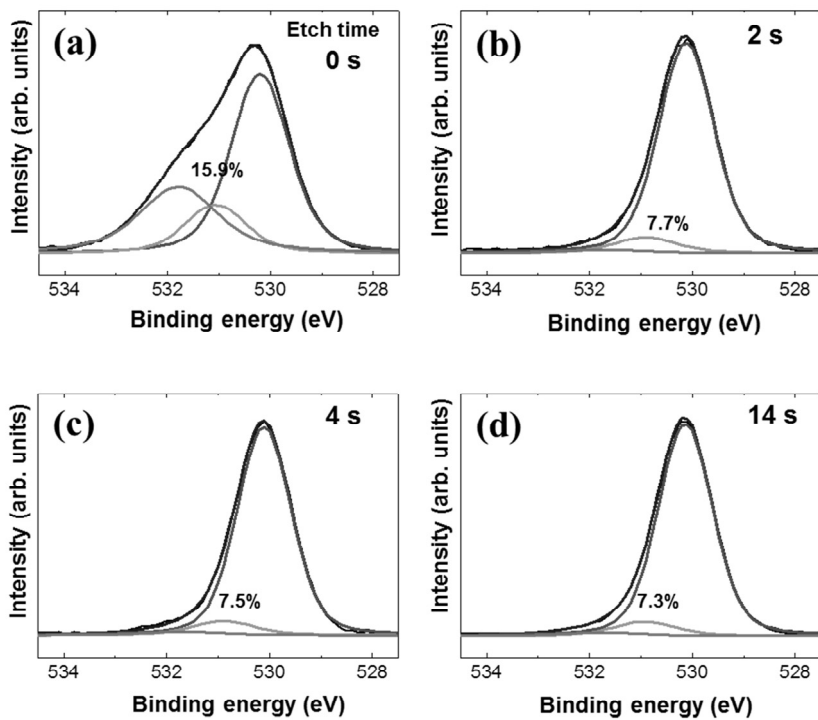


Fig. 4.2.7. The evolution of deconvoluted O *1s* XPS spectra of the 300 s-treated ZTO films as a function of XPS etch time.

Table 4.2.3. Comparison of portion of the O *1s* peaks deconvoluted from the XPS spectra of the untreated and 300 s-treated ZTO films as a function of XPS etch time.

(a) Untreated ZTO film

XPS Etch time	O <i>1s</i> peak [eV]		
	Lattice Oxygen (530.20 ± 0.04)	Oxygen deficient (531.06)	Hydroxyl (531.89)
0 s	0.549	0.224	0.227
2 s	0.885	0.098	0.017
4 s	0.887	0.099	0.013
14 s	0.901	0.077	0.021

(b) 300 s ozone treated ZTO film

XPS Etch time	O <i>1s</i> peak [eV]		
	Lattice Oxygen (530.20 ± 0.04)	Oxygen deficient (531.06)	Hydroxyl (531.89)
0 s	0.551	0.159	0.289
2 s	0.901	0.077	0.021
4 s	0.901	0.075	0.024
14 s	0.904	0.073	0.023

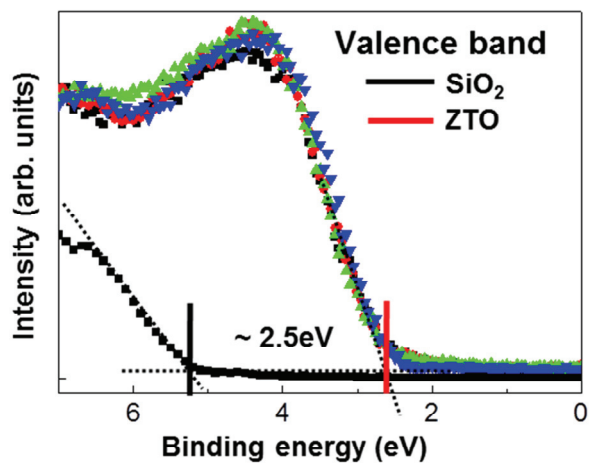


Fig. 4.2.8. The valence band (VB) XPS of SiO₂ insulator (black line), untreated ZTO film, 30 s ozone treated, 300 s ozone treated, and 600 s ozone treated ZTO films.

The photo-desorption mechanism can also be considered as a possible reason for the negative V_{th} shift under NBIS duration.⁵⁰ Because the change in surface coverage with OH groups can affect the number of desorbed oxygen species on the ZTO surface during NBIS duration, it is necessary to discuss the plausibility of O_2 photo-desorption on the channel surface. Figure 4.2.9 shows the FTIR absorbance spectra of the ZTO films as a function of the O_3 treatment time. The broad peak in the range, 3000-3750 cm^{-1} , can be assigned to O-H stretching vibrations.^{80,81} The untreated ZTO film contained appreciable O-H bonding, which can be reasonable from the adsorption of oxygen during the PDA process. The peak in the range of 3000-3750 cm^{-1} increased gradually with increasing O_3 treatment time, indicating an increase in the total amount of hydroxyl bonding with increasing O_3 treatment. Weakly chemisorbed oxygen species, such as O_2^- on the ZTO surface can be desorbed by photon exposure during NBIS duration.^{27,28} The photon-induced desorption of O_2^- or OH^- from the back surface of the channel liberates the electron carrier into the channel, which was trapped by the chemisorbed species. This eventually increases the carrier concentration of the channel, which induces the V_{th} in the negative voltage direction. Figure 4.2.10 shows the energy diagram of various oxygen species in the gas phase, adsorbed at the surface and within the lattice of a binary metal oxide. Among O_2^- and OH^- , OH^- is assumed to have a higher binding energy to the surface, so that a surface with a higher density of OH^-

is more immune to photo-desorption and would show better NBIS stability. The adsorption of O_2^- and OH^- would occur preferentially at surface defect sites, such as V_O , as depicted in Fig. 4.2.11. Figure 4.2.11 shows the process occurring on the ZTO surface during the ozone treatment. At room temperature, the balance of the O_2^- coverage with O_2 gas is approached slowly. On tin oxide films the reaction adsorbed $O_2^- + e^- = 2 O^-$ takes place with increasing the temperature from electron paramagnetic resonance (EPR) studies.⁵¹ Above approximately 200 °C, O^- ions are found as the prevailing species. When, no O_3 treatment was performed, there could be a non-negligible amount of adsorbed O_2^- compared to OH^- species suggesting that this sample is prone to photo-desorption, and hence NBIS instability as shown in Fig. 4.2.10. On the other hand, when the ZTO surface was treated with chemically active ozone, the weakly bound O_2^- would be replaced with OH^- , as illustrated in Fig. 4.2.11(a) and (c). At temperatures $> \sim 200$ °C O_3 decomposes to an O_2 molecule and active oxygen radicals.⁸² The termination of an OH group by a UV- O_3 treatment or plasma treatment on the oxide film is frequently reported.^{69,83-85} Oxygen radicals adsorb strongly to the oxide surface and are transformed easily to OH species through an interaction with air. OH takes electrons from the channel to form OH^- , which improves the channel properties. Figure 4.2.12 shows the process occurring on the ZTO surface during the NBIS test. Overall, the ozone treatment converts the surface adsorption species from weakly bound O_2^- species to highly

chemisorbed OH^- at the surface V_O site, which in turn suppresses the photo-desorption process because the chemisorbed OH^- species have a higher binding energy than O_2^- species.²⁸

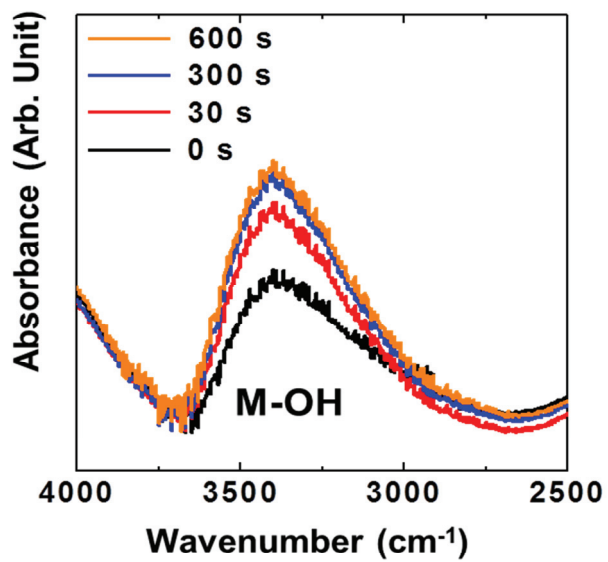


Fig. 4.2.9. FTIR spectra of untreated ZTO film, 30 s ozone treated, 300 s ozone treated, and 600 s ozone treated ZTO films.

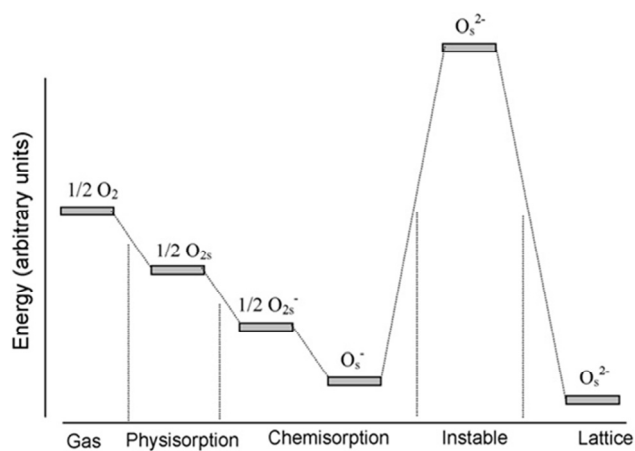


Fig. 4.2.10. The energy diagram of various oxygen species in the gas phase, adsorbed at the surface and within the lattice of a binary metal oxide. [23,24]

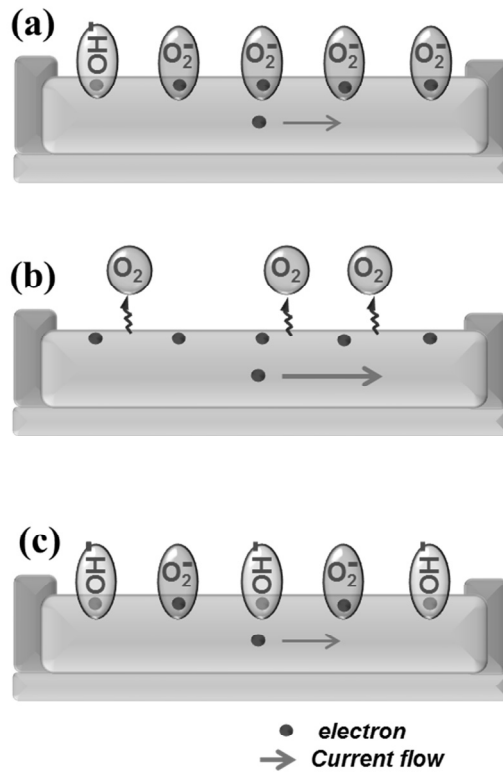


Fig. 4.2.11. Process occurring on the ZTO surface during the ozone treatment. (a) air annealing (b) vacuum chamber (c) ozone treated ZTO films.

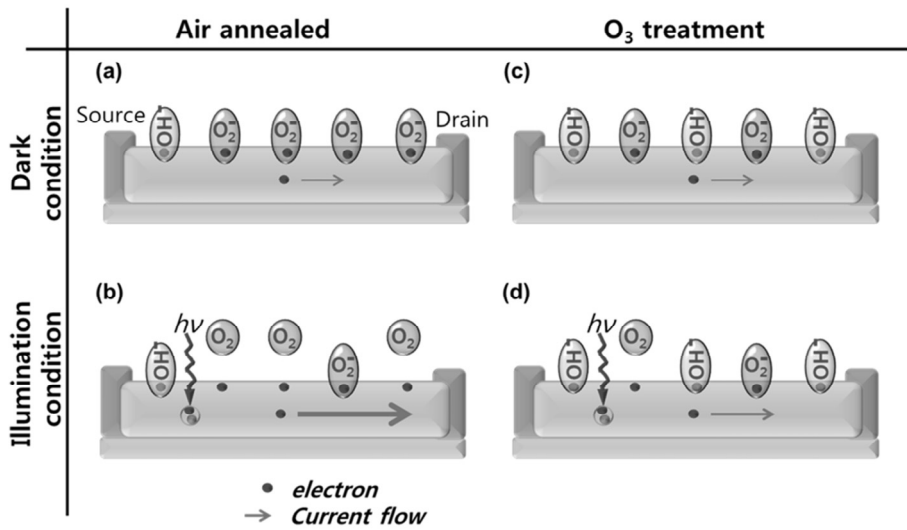


Fig. 4.2.12. Process occurring on the ZTO surface during the NBIS test.

The amount of weakly bounded oxygen removed by the ozone treatment can be estimated as follows under a rather crude assumption that the ΔV_{th} was totally induced by photo-desorption, and OH^- species do not desorb during the NBIS test. The NBIS-induced negative ΔV_{th} was ~ 4.2 V for the untreated ZTO FETs. In contrast, the 600 s O_3 treated device exhibited a negligible ΔV_{th} of -0.07 V, which suggests that the O_3 treatment on the ZTO surface causes the substitution of weakly bounded O_2^- species by strong chemisorbed OH^- species. Under the assumptions mentioned above, the total number of photo-desorbed oxygen was calculated to be $8.5 \times 10^{11} / \text{cm}^2$ using the formula, charge variation (Q_{des}) = gate insulator capacitance (C_i) \times ΔV_{th} . Under the NBIS condition, the ZTO layer is fully depleted, so that the total capacitance must be composed of the series capacitance of gate insulator (C_i) and semiconductor (C_s). In order to estimate the C_s , metal ($p^{++}\text{Si}$) - insulator (SiO_2) - semiconductor (ZTO) structure was fabricated and the depletion capacitance was measured (data not shown). The result showed that the estimated dielectric constant of ZTO is consistent with the calculated value using parameters from literatures.^{86,87} The measured C_i is much lower than C_s so that the total capacitance can be approximated to C_i . Considering that the film density and molar weight of ZTO are 5.05 g/cm^3 and 232.0 g/mol , respectively, the concentration of surface oxygen is approximated to $1.2 \times 10^{15} / \text{cm}^2$.⁸ Therefore, the maximum portion of responsible desorption sites of weakly bounded O_2^- species can be

estimated to be $\sim 0.1\%$. The above model was examined further by investigating the water wetting properties of O_3 treated ZTO films. Figure 4.2.13 shows the change in the water contact angle (WCA) as a function of the ozone treatment time. Although the WCA of the untreated sample was 38.7° , the 600 s-treated ZTO film showed a WCA of 15.2° , indicating that the O_3 treatment makes the film surface more hydrophilic. This is consistent with the aforementioned postulation because the hydrophilicity of the O_3 treated films is due to the higher number of polar groups, such as OH.⁶⁹ The WCA decreased drastically during the initial O_3 treatment of 30 s. This decrease in WCA corresponds to an increase in the OH concentration on the ZTO surface. In Fig. 4.2.3, the negative V_{th} shift for the 30 s-treated ZTO FET after applying NBIS for 3000 s was suppressed from 4.2 V (untreated ZTO FET) to 0.57 V. Therefore, the passivation kinetics of the surface V_O defect with OH groups by the O_3 treatment appears to be quite fast (~ 30 sec). The relative decreases in the bulk $[V_O]$ for the 30 s and 600 s-treated ZTO films were $\sim 3.8\%$ and 9.2% , respectively (see Table 4.2.2). Therefore, the improvement in the NBIS stability of ZTO FET originates from the curing process of weakly bound oxygen defect sites during the initial O_3 treatment (~ 30 sec). The long time O_3 treatment (~ 600 sec) further facilitates the annihilation of $[V_O]$ in the ZTO bulk film, which is responsible for the excellent stability of the 600 s-treated ZTO FET. The physical properties of films like the surface roughness could affect water contact angle and the

amount of surface adsorption species. In order to verify this model, the film characterization of the different ZTO thin films was investigated. Figure 4.1.14 depict the surface morphology, obtained by atomic force microscopy, for the untreated ZTO film, 30 s ozone treated, 300 s ozone treated, and 600 s ozone treated ZTO films. The root-mean-square (rms) roughness for the ZTO film was not affected by the ozone treatment. Both films exhibited the same rms roughness of ~ 0.3 nm. From XRD measurement, the crystallographic structure of the ZTO film was also independent of the ozone treatment (not shown). Both films were amorphous. Figure 4.1.15 shows the XRR data for the different ZTO films as a function of the ozone treatment time. The film densities obtained from the XRR simulation result were ~ 5.05 g/cm³ for the both ZTO films, respectively. The film densities were also independent of the ozone treatment time.

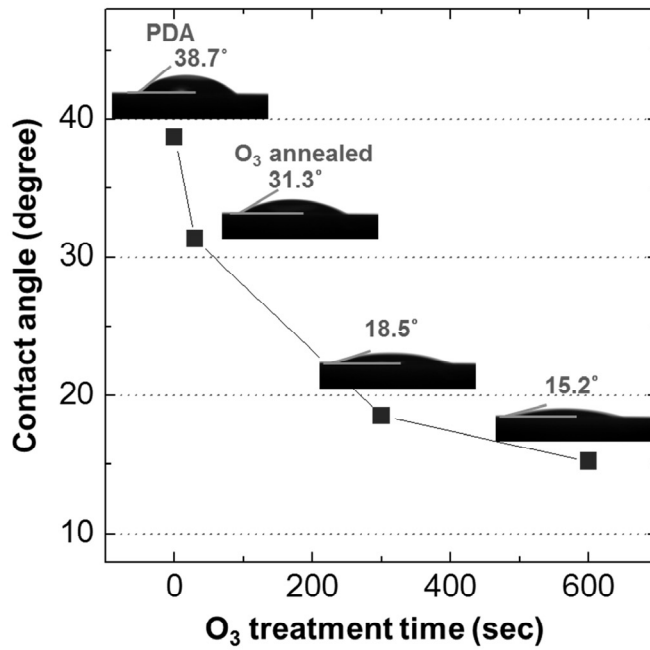


Fig. 4.2.13. Variations in contact angle of water droplets of ZTO films with different O₃ treatment times.

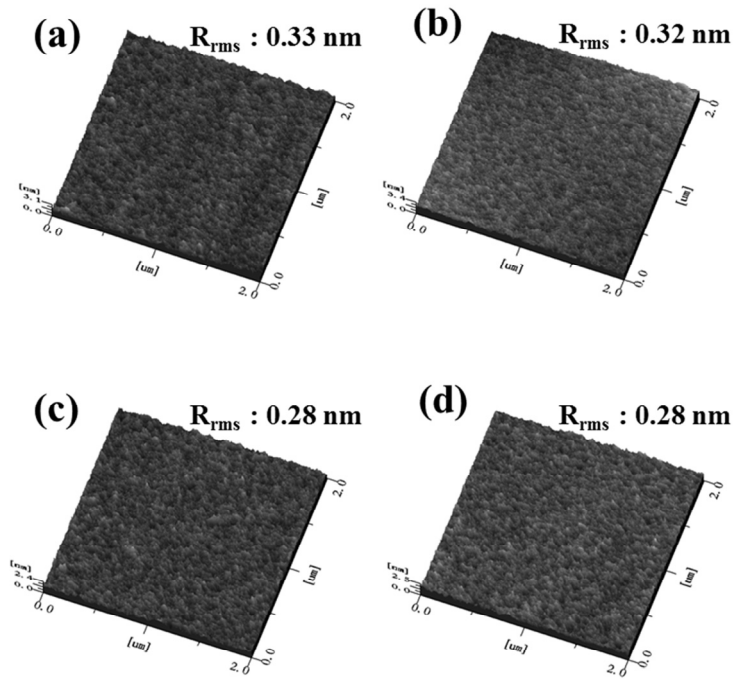


Fig. 4.2.14. AFM images ($2 \mu\text{m} \times 2 \mu\text{m}$) of (a) untreated ZTO film, (b) 30 s ozone treated, (c) 300 s ozone treated, and (d) 600 s ozone treated ZTO films.

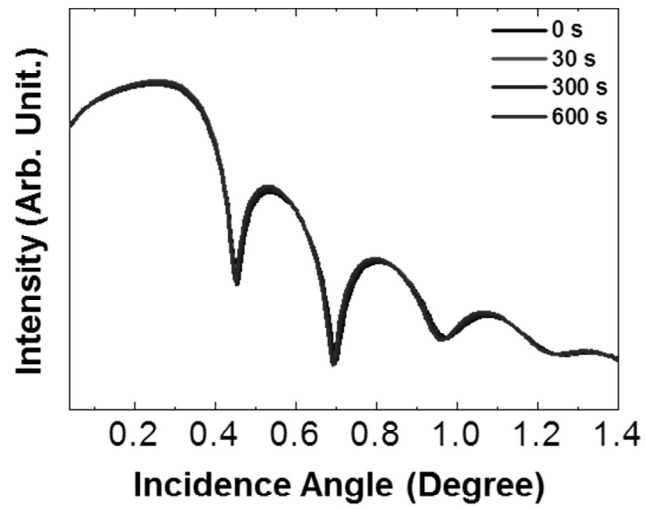


Fig. 4.2.15. The X-ray reflectivity spectrum for the ZTO films with different O₃ treatment times.

Finally, relative contribution of two degradation mechanisms to the overall NBIS-induced V_{th} instability is estimated. In estimation, two types of encapsulated devices were prepared to prevent the photo induced adsorption and desorption of O_2^- ions from the ZTO surface. First, a 13-nm-thick Al_2O_3 film was deposited on the ZTO surface by atomic layer deposition (ALD) with $Al(CH_3)_3$ and ozone as the Al-precursor and oxygen source, respectively, at a substrate temperature of 210 °C. Corresponding NBIS-induced V_{th} shift is shown in Fig. 4.2.16(a), where V_{th} shift of 0.39 V was achieved after NBIS of 3,000 s. Around 90% decrease in the V_{th} shift from the Al_2O_3 passivation, compared to that of unpassivated sample, indicates that photo-desorption of oxygen atoms was the dominant factor to cause instability in TFTs. However, the presence of highly reactive ozone during the ALD process could have affected the bulk defect density of the ZTO channel layer. In order to neglect such effect from the ALD process, the polymer passivation layer on ZTO TFT was formed by a spin coating method. In this case, a standard photoresist was used as the polymer passivation layer. The NBIS-tested transfer characteristics are shown in Fig. 4.2.16(b). The V_{th} shift after 3,000 s was 0.73 V, suggesting ~ 85% of the degradation was induced by the photo-desorption. These results suggest that the photo-induced adsorption and desorption on the back channel surface of the TFT play dominant role in the V_{th} shift during the NBIS test.

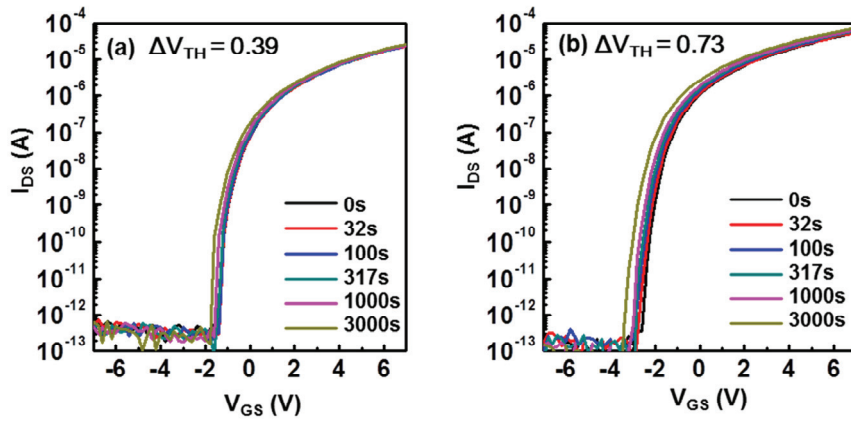


Fig. 4.2.16. Evolution of the transfer characteristics for (a) the Al_2O_3 passivated and (b) polymer passivated ZTO TFT as a function of the applied NBIS time.

4.1.4 Summary

This study examined the effect of O₃ treatment on the instability of the ZTO FETs using a NBIS test. The untreated ZTO FETs suffered from a huge negative V_{th} shift of 4.2 V, whereas the O₃ treated device exhibited the much superior stability under NBIS conditions with increasing O₃ treatment time. The V_{th} value of the 600 s-treated ZTO FET was relatively constant ($\Delta V_{th} = -0.07$ V) after the application of identical NBIS. The chemical state of the O₃ treated ZTO thin film was analyzed systematically by XPS, FTIR and contact angle measurements. The V_O concentration in the ZTO thin film decreased gradually with increasing O₃ treatment time. This suggests that the V_{th} shift of ZTO films under NBIS conditions is due partly to the transition of V_O to V_O²⁺ by light excitation. Therefore, an O₃ treatment can enhance the in-diffusion of oxygen radicals and reduce the [V_O] defect density in the ZTO film, resulting in an improvement in photo-bias reliability. Simultaneously, the number of hydroxyl groups on the surface of the ZTO film increased with increasing O₃ treatment time. This suggests another reason for the improved NBIS stability of ZTO FETs: the substitution of weakly bound O₂⁻ species at the surface V_O defect sites with OH. This suggests that the surface condition of ZTO films is an important factor determining the photo-bias stability of metal oxide FETs.

Chapter 5. Conclusions

The effect of the negative bias illumination stress on the electrical properties of Zinc Tin Oxide thin film transistor was studied.

TFT with ZrO_2 incorporated ZTO channel layer was fabricated. And the effect of ZrO_2 incorporation in the ZTO film and field effect transistors (TFT) was investigated. As the ZrO_2 content increases, the μ_{FE} and V_{th} values were diminished and increased, respectively, which was attributed to the increase in R_C . However, in terms of the negative bias illumination stress (NBIS) instability, the Zr-incorporated ZTZO device exhibited much better photo-stability. While the ZTO device exhibited inferior V_{th} stability ($\Delta V_{th} = -12.5$ V) after the application of NBIS for 5,000 s, the stability ($\Delta V_{th} = -4.2$ V) of the ZTZO (ZrO_2 doped ZTO) device against NBIS was greatly improved, which was attributed to the reduction of the $[V_O]$ defect density in the ZTZO film. The relative area of the oxygen vacancy-related peak decreased with increasing ZrO_2 fraction in the ZTZO film. The decreasing proportion of the peak area corresponding to oxygen vacancies with increasing ZrO_2 content strongly indicates that the improvement of the photo-stability for the higher content ZrO_2 devices under NBS conditions arose from the reduction of the V_O defect density. Therefore, the photo-transition model of V_O is consistent with the XPS results. This is thought to be related to the fact that the Gibbs free energies of formation (ΔG_f) for ZnO,

SnO, SnO₂ and ZrO₂. The most negative ΔG_f value (-1039.7 kJ/mole) of ZrO₂ suggests that the chemical bonding with respect to oxygen atoms is the strongest among the Zn, Sn and Zr cation atoms. Thus, increasing the Zr content in the ZTO system will decrease the density of V_O. The photo-desorption mechanism can also be considered as a reason for the V_{th} shift under instability stress conditions. The change in surface coverage with OH groups can affect the number of desorbed oxygen species on the ZTO surface during instability stress duration. This suggests that the surface region of ZTO films is an important factor determining the photo-bias stability of metal oxide TFTs.

In addition, the effect of O₃ treatment on the instability of the ZTO FETs was examined using a NBIS test. The untreated ZTO FETs suffered from a huge negative V_{th} shift of 4.2 V, whereas the O₃ treated device exhibited the much superior stability under NBIS conditions with increasing O₃ treatment time. The V_{th} value of the 600 s-treated ZTO FET was relatively constant ($\Delta V_{th} = -0.07$ V) after the application of identical NBIS. The chemical state of the O₃ treated ZTO thin film was analyzed systematically by XPS, FTIR and contact angle measurements. The V_O concentration in the ZTO thin film decreased gradually with increasing O₃ treatment time. This suggests that the V_{th} shift of ZTO films under NBIS conditions is due partly to the transition of V_O to V_O²⁺ by light excitation. Therefore, an O₃ treatment can enhance the in-diffusion of oxygen radicals

and reduce the $[V_O]$ defect density in the ZTO film, resulting in an improvement in photo-bias reliability. Simultaneously, the number of hydroxyl groups on the surface of the ZTO film increased with increasing O_3 treatment time. This suggests another reason for the improved NBIS stability of ZTO FETs: the substitution of weakly bound O_2^- species at the surface V_O defect sites with OH.

Finally, relative contribution of two degradation mechanisms to the overall NBIS-induced V_{th} instability is estimated. In estimation, two types of encapsulated devices with Al_2O_3 film and polymer were prepared to prevent the photo induced adsorption and desorption of O_2^- ions from the ZTO surface. Around 85% ~ 90% decrease in the V_{th} shift from the two types of encapsulated devices, compared to that of unpassivated sample, indicates that photo-desorption of oxygen atoms was the dominant factor to cause instability in ZTO based TFTs.

From these results, the incorporation of an optimal amount of doping materials into ZTO TFTs can provide a means to overcome the problem of NBIS instability. In addition, the surface treatment method related to the chemical adsorption/desorption on the back surface of the channel can be an important factor to improve the photo-bias stability of metal oxide FET to be used in AMLCDs, AMOLEDs and flexible/transparent electronics.

References

- 1 Y. He, R. Hattori, and J. Kanicki, *Electron Device Letters*, IEEE **21**, 590 (2000).
- 2 K. Yoneda, R. Yokoyama, and T. Yamada, in *Development trends of LTPS TFT LCDs for mobile applications*, 2001 (IEEE), p. 85.
- 3 N. K. Song, M. S. Kim, S. H. Han, Y. S. Kim, and S. K. Joo, *Electron Devices*, IEEE Transactions on **54**, 1420 (2007).
- 4 A. Choi, T. Ghong, Y. Kim, J. Oh, and J. Jang, *Journal of Applied Physics* **100**, 113529 (2006).
- 5 J. H. Oh, E. H. Kim, S. K. Kim, J. H. Cheon, Y. D. Son, and J. Jang, *Applied Physics Letters* **87**, 231120 (2005).
- 6 J. H. Lee, J. H. Kim, and M. K. Han, *Electron Device Letters*, IEEE **26**, 897 (2005).
- 7 B. S. Yang, S. Park, S. Oh, Y. J. Kim, J. K. Jeong, C. S. Hwang, and H. J. Kim, *J. Mater. Chem.* **22**, 10994 (2012).
- 8 B. S. Yang, M. S. Huh, S. Oh, U. S. Lee, Y. J. Kim, M. S. Oh, J. K. Jeong, C. S. Hwang, and H. J. Kim, *Applied Physics Letters* **98**, 122110 (2011).
- 9 H. Uchida, K. Takechi, S. Nishida, and S. Kaneko, *Japanese Journal of Applied Physics* **30**, 3691 (1991).
- 10 H. Kuriyama, S. Kiyama, S. Noguchi, T. Kuwahara, S. Ishida, T. Nohda, K. Sano, H. Iwata, S. Tsuda, and S. Nakano, in *High*

mobility poly-Si TFT by a new excimer laser annealing method for large area electronics, 1991 (IEEE), p. 563.

- 11 T. Kamiya, K. Nomura, and H. Hosono, *Science and Technology of Advanced Materials* **11**, 044305 (2010).
- 12 D. Hong and J. F. Wager, *Journal of Vacuum Science & Technology B: Microelectronics and Nanometer Structures* **23**, L25 (2005).
- 13 H. Q. Chiang, PhD thesis, Oregon State University (2007).
- 14 K. Chopra, S. Major, and D. Pandya, *Thin Solid Films* **102**, 1 (1983).
- 15 K. Narayanan, R. Rajaraman, M. Valsakumar, K. Nair, and K. Vijayakumar, *Materials research bulletin* **34**, 1729 (1999).
- 16 J. F. Wager, *Science* **300**, 1245 (2003).
- 17 S. Masuda, K. Kitamura, Y. Okumura, S. Miyatake, H. Tabata, and T. Kawai, *Journal of Applied Physics* **93**, 1624 (2003).
- 18 R. Hoffman, B. J. Norris, and J. Wager, *Applied Physics Letters* **82**, 733 (2003).
- 19 R. Presley, C. Munsee, C. Park, D. Hong, J. Wager, and D. Keszler, *Journal of Physics D: Applied Physics* **37**, 2810 (2004).
- 20 K. Ellmer, *Journal of Physics D: Applied Physics* **34**, 3097 (2001).
- 21 Ç. Kılıç and A. Zunger, *Physical Review Letters* **88**, 95501 (2002).
- 22 Y. Kuo, *Thin Film Transistors: Amorphous silicon thin film*

- transistors*, Vol. 1 (Kluwer Academic Pub, 2004).
- 23 E. Fortunato, P. Barquinha, and R. Martins, *Advanced Materials* (2012).
 - 24 S. Yamamoto and M. Mitaka, *JAPANESE JOURNAL OF APPLIED PHYSICS PART 1 REGULAR PAPERS SHORT NOTES AND REVIEW PAPERS* **32**, 462 (1993).
 - 25 Y. Uchida and M. Matsumura, *Electron Devices, IEEE Transactions on* **36**, 2940 (1989).
 - 26 C. R. Kagan and P. Andry, *Thin-film transistors* (CRC Press, 2003).
 - 27 Y. Takahashi, M. Kanamori, A. Kondoh, H. Minoura, and Y. Ohya, *Japanese Journal of Applied Physics* **33**, 6611 (1994).
 - 28 T. Seiyama, *Chemical sensor technology*, vol. 1, Kodansha/Elsevier.
 - 29 D. K. Schroder, *Semiconductor material and device characterization* (Wiley-IEEE press, 2006).
 - 30 A. Ortiz-Conde, F. J. G. Sánchez, and M. Guzmán.
 - 31 J. K. Jeong, J. H. Jeong, H. W. Yang, T. K. Ahn, M. Kim, K. S. Kim, B. S. Gu, H.-J. Chung, J.-S. Park, Y.-G. Mo, H. D. Kim, and H. K. Chung, *Journal of the Society for Information Display* **17**, 95 (2009).
 - 32 E. Fortunato, P. Barquinha, A. Pimentel, A. M. F. Gonçalves, A. J. S. Marques, L. Pereira, and R. F. P. Martins, *Advanced Materials* **17**, 590 (2005).

- 33 K. Nomura, H. Ohta, A. Takagi, T. Kamiya, M. Hirano, and H. Hosono, *Nature* **432**, 488 (2004).
- 34 K. S. Son, H. S. Kim, W. J. Maeng, J. S. Jung, K. H. Lee, T. S. Kim, J. S. Park, J. Y. Kwon, B. Koo, and S. Y. Lee, *Electron Device Letters, IEEE* **32**, 164 (2011).
- 35 J. M. Lee, I. T. Cho, J. H. Lee, and H. I. Kwon, *Applied Physics Letters* **93**, 093504 (2008).
- 36 A. Suresh and J. Muth, *Applied Physics Letters* **92**, 033502 (2008).
- 37 K. Nomura, T. Kamiya, M. Hirano, and H. Hosono, *Applied Physics Letters* **95**, 013502 (2009).
- 38 J. K. Jeong, H. W. Yang, J. H. Jeong, Y. G. Mo, and H. D. Kim, *Applied Physics Letters* **93**, 123508 (2008).
- 39 S. Yang, D. H. Cho, M. K. Ryu, S. H. K. Park, C. S. Hwang, J. Jang, and J. K. Jeong, *Electron Device Letters, IEEE* **31**, 144 (2010).
- 40 J. Lee, J. S. Park, Y. S. Pyo, D. B. Lee, E. H. Kim, D. Stryakhilev, T. W. Kim, D. U. Jin, and Y. G. Mo, *Applied Physics Letters* **95**, 123502 (2009).
- 41 J. H. Shin, J. S. Lee, C. S. Hwang, S. H. K. Park, W. S. Cheong, M. Ryu, C. W. Byun, J. I. Lee, and H. Y. Chu, *ETRI Journal* **31**, 62 (2009).
- 42 K. H. Ji, J. I. Kim, Y. G. Mo, J. H. Jeong, S. Yang, C. S. Hwang, S.

- H. K. Park, M. K. Ryu, S. Y. Lee, and J. K. Jeong, *Electron Device Letters*, IEEE **31**, 1404 (2010).
- 43 J. H. Kim, U. K. Kim, Y. J. Chung, and C. S. Hwang, *Applied Physics Letters* **98**, 232102 (2011).
- 44 J. H. Kim, U. K. Kim, Y. J. Chung, and C. S. Hwang, *physica status solidi (RRL)—Rapid Research Letters* (2011).
- 45 Y. J. Chung, J. H. Kim, U. K. Kim, S. H. Rha, and C. S. Hwang, *Journal of Applied Physics* (**accepted**) (2011).
- 46 M. D. H. Chowdhury, P. Migliorato, and J. Jang, *Applied Physics Letters* **97**, 173506 (2010).
- 47 S. Yang, K. Hwan Ji, U. Ki Kim, C. Seong Hwang, S.-H. Ko Park, C.-S. Hwang, J. Jang, and J. Kyeong Jeong, *Applied Physics Letters* **99**, 102103 (2011).
- 48 J. Y. Kwon, J. S. Jung, K. S. Son, K. H. Lee, J. S. Park, T. S. Kim, R. Choi, J. K. Jeong, and B. Koo, *Applied Physics Letters* **97**, 183503 (2010).
- 49 K. H. Ji, J.-I. Kim, H. Y. Jung, S. Y. Park, R. Choi, U. K. Kim, C. S. Hwang, D. Lee, H. Hwang, and J. K. Jeong, *Applied Physics Letters* **98**, 103509 (2011).
- 50 P.-T. Liu, Y.-T. Chou, and L.-F. Teng, *Applied Physics Letters* **95**, 233504 (2009).
- 51 S. C. Chang, *Journal of Vacuum Science and Technology* **17**, 366

- (1980).
- 52 J. F. Conley Jr, Device and Materials Reliability, IEEE Transactions on, 1 (2010).
- 53 M. S. Huh, B. S. Yang, J. Song, J. Heo, S. J. Won, J. K. Jeong, C. S. Hwang, and H. J. Kim, Journal of The Electrochemical Society **156**, J6 (2009).
- 54 R. Popovic, (Adam Hilger, Bristol, 1991).
- 55 K. H. Lee, J. S. Jung, K. S. Son, J. S. Park, T. S. Kim, R. Choi, J. K. Jeong, J. Y. Kwon, B. Koo, and S. Lee, Applied Physics Letters **95**, 232106 (2009).
- 56 H. Oh, S.-M. Yoon, M. K. Ryu, C.-S. Hwang, S. Yang, and S.-H. K. Park, Applied Physics Letters **97**, 183502 (2010).
- 57 M. D. H. Chowdhury, P. Migliorato, and J. Jang, Applied Physics Letters **97**, 173506 (2010).
- 58 S. Yang, D.-H. Cho, M. K. Ryu, S.-H. K. Park, C.-S. Hwang, J. Jang, and J. K. Jeong, Applied Physics Letters **96**, 213511 (2010).
- 59 T. C. Fung, K. Abe, H. Kumomi, and J. Kanicki, Journal of Display Technology **5**, 452 (2009).
- 60 H. S. Seo, J. U. Bae, D. H. Kim, Y. J. Park, C. D. Kim, I. B. Kang, I. J. Chung, J. H. Choi, and J. M. Myoung, Electrochemical and Solid-State Letters **12**, H348 (2009).
- 61 P. T. Liu, Y. T. Chou, and L. F. Teng, Applied Physics Letters **95**,

- 233504 (2009).
- 62 B. Ryu, H. K. Noh, E. A. Choi, and K. Chang, *Applied Physics Letters* **97**, 022108 (2010).
- 63 S. Lany and A. Zunger, *Physical Review B* **72**, 035215 (2005).
- 64 A. Janotti and C. G. Van de Walle, *Physical Review B* **76**, 165202 (2007).
- 65 R. Cross and M. De Souza, *Applied Physics Letters* **89**, 263513 (2006).
- 66 Y. Jeong, C. Bae, D. Kim, K. Song, K. Woo, H. Shin, G. Cao, and J. Moon, *ACS Applied Materials & Interfaces* **2**, 611 (2010).
- 67 S. J. Seo, C. G. Choi, Y. H. Hwang, and B. S. Bae, *Journal of Physics D: Applied Physics* **42**, 035106 (2009).
- 68 I. Bahn, *Exergy* **1**, 29 (1989).
- 69 R. Wang, N. Sakai, A. Fujishima, T. Watanabe, and K. Hashimoto, *The Journal of Physical Chemistry B* **103**, 2188 (1999).
- 70 S. K. Park, Y. H. Kim, H. S. Kim, and J. I. Han, *Electrochemical and Solid-State Letters* **12**, H256 (2009).
- 71 J. S. Park, J. K. Jeong, H. J. Chung, Y. G. Mo, and H. D. Kim, *Applied Physics Letters* **92**, 072104 (2008).
- 72 K. S. Son, T. S. Kim, J. S. Jung, M. K. Ryu, K. B. Park, B. W. Yoo, K. C. Park, J. Y. Kwon, S. Y. Lee, and J. M. Kim, *Electrochemical and Solid-State Letters* **12**, H26 (2009).

- 73 M. K. Ryu, S. Yang, S.-H. K. Park, C.-S. Hwang, and J. K. Jeong, *Applied Physics Letters* **95**, 173508 (2009).
- 74 C. Avis and J. Jang, *Journal of Materials Chemistry* **21**, 10649 (2011).
- 75 Y. Dai, P. Wu, L. Dai, X. Fang, and G. Qin, *Journal of Materials Chemistry* **21**, 2858 (2011).
- 76 B. Ryu, H.-K. Noh, E.-A. Choi, and K. J. Chang, *Applied Physics Letters* **97**, 022108 (2010).
- 77 S. Lany and A. Zunger, *Physical Review B* **72** (2005).
- 78 M. G. Kim, H. S. Kim, Y. G. Ha, J. He, M. G. Kanatzidis, A. Facchetti, and T. J. Marks, *Journal of the American Chemical Society* (2010).
- 79 A. Janotti and C. G. Van de Walle, *Physical Review B* **76** (2007).
- 80 G. Socrates, *Infrared characteristic group frequencies : tables and charts* Socrates, Wiley.
- 81 K. Song, Y. Jung, Y. Kim, A. Kim, J. K. Hwang, M. M. Sung, and J. Moon, *Journal of Materials Chemistry* **21**, 14646 (2011).
- 82 L. Berry and J. Brunet, *Sensors and Actuators B: Chemical* **129**, 450 (2008).
- 83 X. Q. Meng, D. X. Zhao, J. Y. Zhang, D. Z. Shen, Y. M. Lu, L. Dong, Z. Y. Xiao, Y. C. Liu, and X. W. Fan, *Chemical Physics Letters* **413**, 450 (2005).

- 84 Ren-De Sun, A. Nakajima, A. Fujishima, T. Watanabe, and K. Hashimoto, *The Journal of Physical Chemistry B* **105**, 1984 (2001).
- 85 X. Feng, L. Feng, M. Jin, J. Zhai, L. Jiang, and D. Zhu, *Journal of the American Chemical Society* **126**, 62 (2004).
- 86 J. F. McAleer, P. T. Moseley, J. O. W. Norris, and D. E. Williams, *J. Chem. Soc., Faraday Trans. 1* **83**, 1323 (1987).
- 87 H. J. Chung, J. H. Jeong, T. K. Ahn, H. J. Lee, M. Kim, K. Jun, J. S. Park, J. K. Jeong, Y. G. Mo, and H. D. Kim, *Electrochemical and Solid-State Letters* **11**, H51 (2008).

Curriculum Vitae

Bong Seob Yang

Department of Materials Science and Engineering
College of Engineering, Seoul National University
San 56-1 Silim-dong, Gwanak-gu, Seoul, 151-742, Korea

Tel: +82-02-880-7378

Fax: +82-02-874-7626

E-mail: Yang3@snu.ac.kr

EDUCATION

M.S. & Ph. D. course, Department of Materials Science and Engineering

*Seoul National University, Seoul, Korea
2007. 3 – 2012. 8*

B.S., Department of Materials Science and Engineering

*Seoul National University, Seoul, Korea
2000. 3 – 2007. 2*

RESEARCH AREAS

1. Transparent Thin film Transistor for display application

- Fabrication and electrical characterization of TFTs based on Amorphous Oxide semiconductor and transparent electrode for large scale and high resolution display.
- Research for the improvement in reliability of TFTs

TECHNICAL SKILLS

1. Deposition methods

- **RF and DC magnetron sputtering** for various oxide and metal films deposition.
- **E-beam evaporation** for metal electrodes

2. Device fabrication methods

- **MIS capacitor** structures for electrical characterization of the dielectric films
- **TFT structures** by using shadow mask via sputtering method
- TFT patterned by MA6-II aligner for **photolithography** (ultra violet)

3. Analysis methods

- **Transfer characterization** and **reliability** evaluation of TFTs
- HP4194A for C-V measurement of MIS capacitors
- Keithley 4200, HP4145B and HP4155A for I-V measurement of TFTs, MIS capacitors
- **Ellipsometer** for film thickness measurement
- **Hall measurement** and **4 point probe**
- **Fourier Transformed Infrared (FTIR)**
- **Atomic Force Microscopy (AFM, JEOL, JSPM-5200)**
- **X-ray diffraction (XRD)**

4. Furnace for ambient and vacuum annealing

Research Project

1. “Technology development of Oxide thin film transistor for next generation LCD”, from Samsung electronics co., Korea, 06/2008 – 05/2010.

List of publication

1. Journals (SCI)

1.1 International

1. Myung Soo Huh, **Bong Seop Yang**, Jaewon Song, Jaeyeong Heo, Seok-Jun Won, Jae Kyeong Jeong, Cheol Seong Hwang, and Hyeong Joon Kim, "Improving the Morphological and Optical Properties of Sputtered Indium Tin Oxide Films by Adopting Ultralow-Pressure Sputtering", *J. Electrochem. Soc.*, **156** (1) J6-J11 (2009).
2. Myung Soo Huh, **Bong Seop Yang**, Joohei Lee, Jaeyeong Heo, Sang Jin Han, Kapsoo Yoon, Sung-Hoon Yang, Cheol Seong Hwang, Hyeong Joon Kim, "Improved electrical properties of tin-oxide films by using ultralow-pressure sputtering process", *Thin Solid Films*, **518** 1170-1173 (2009).
3. Myung Soo Huh, **Bong Seop Yang**, Seungha Oh, Joohei Lee, Kapsoo Yoon, Jae Kyeong Jeong, Cheol Seong Hwang, and Hyeong Joon Kim, "Improvement in the Performance of Tin Oxide Thin film Transistors by Alumina Doping", *Electrochem. Solid-State Lett.*, **12**(10) H385-H387 (2009).
4. Seung Wook Ryu, Jong Ho Lee, Young Bae Ahn, Choon Hwan Kim, **Bong Seob Yang**, Gun Hwan Kim, Soo Gil Kim, Se-Ho Lee, Cheol Seong Hwang, and Hyeong Joon Kim, "The reason for the increased threshold switching voltage of SiO₂ doped Ge₂Sb₂Te₅ thin films for phase change random access memory", *Appl. Phys. Lett.* **95**, 112110 (2009)

5. Myung Soo Huh, **Bong Seob Yang**, Seungha Oh, Jeong-hwan Kim, Je-Hun Lee, Jae Kyeong Jeong, Cheol Seong Hwang, and Hyeong Joon Kim, "Improving the performance of tin oxide thin film transistors by using ultralow-pressure sputtering", *J. Electrochem. Soc.*, **157**(4) H425-H429 (2010).
6. Myung Soo Huh, Seok-Jun Won, **Bong Seob Yang**, Seungha Oh, Myeong Sook Oh, Jae Kyeong Jeong, and Hyeong Joon Kim, "Improving the performance of thin film transistors with ZnO channel layer fabricated by ultralow-pressure sputtering", *Journal of Vacuum Science and Technology B* 29, 031201 (2011)
7. **Bong Seob Yang**, Myung Soo Huh, Seungha Oh, Ung Soo Lee, Yoon Jang Kim, Myeong Sook Oh, Jae Kyeong Jeong, Cheol Seong Hwang, and Hyeong Joon Kim, "Role of ZrO₂ incorporation in the suppression of negative bias illumination-induced instability in Zn-Sn-O thin film transistors", *Appl. Phys. Lett.* 98, 122110 (2011).
8. Myeong Sook Oh, Myung Soo Huh, **Bong Seob Yang**, Jong Ho Lee, Seong Ha Oh, Ung Soo Lee, Yoon Jang Kim, and Hyeong Joon Kim, "Improvement of electrical and optical properties of molybdenum oxide thin films by ultralow pressure sputtering method", *J. Vac. Sci. Technol. A* 30(3) 031501 (2012)
9. **Bong Seob Yang**, Sanghyun Park, Seungha Oh, Yoon Jang Kim, Jae Kyeong Jeong, Cheol Seong Hwang and Hyeong Joon Kim, "Improvement of the photo-bias stability of the Zn-Sn-O field effect transistors by an ozone treatment", *J. Mater. Chem.*, 2012,22, 10994-10998.
10. Seungha Oh, **Bong Seob Yang**, Yoon Jang Kim, Myeong Sook Oh, Mi Jang, Hoichang Yang, Jae Kyeong Jeong, Cheol Seong Hwang, and Hyeong Joon Kim "Anomalous behavior of negative bias

illumination stress instability in an indium zinc oxide transistor: a cation combinatorial approach”, *Appl. Phys. Lett.*, 2012 (submitted)

2. Proceeding

1. Myung Soo Huh, **Bong Sop Yang**, Seungha Oh, Seok Jun Won, Jae Kyeong Jeong, Cheol Seong Hwang , and Hyeong Joon Kim, “Improvement in the Device Characteristics of Tin Oxide Thin film Transistors by Adopting Ultralow-Pressure Sputtering”, Electrochemical Society, 5-9 October 2009, Vienna, Austria.
2. Myung Soo Huh, **Bong Sop Yang**, Seungha Oh, and Hyeong Joon Kim, “Aluminum doped Tin Oxide based Thin Film Transistors”, The 6th international tin-film transistor conference, 28-29 January, Egret Himeji, Japan.
3. Myung Soo Huh, **Bong Seob Yang**, Seungha Oh, Seok-Jun Won, Sang Jin Han, Cheoi Lae Roh, and Hyeong Joon Kim, “The surface morphological and electrical properties of ultralow-pressure sputtered tin doped indium oxide film”, 2010 53rd SVC annual technical conference, 17-22 April, Orland, Florida, USA.
4. Seungha Oh, **Bong Seob Yang**, Yoon Jang Kim, and Hyeong Joon Kim, “Composition Dependence of the Negative Bias Light Illumination Instability of Indium Zinc Oxide Transistors”, ECS 222nd Meeting, 7-12 October 2012, Honolulu, Hawaii. (accepted)
5. **Bong Seob Yang**, Seungha Oh, Yoon Jang Kim, and Hyeong Joon Kim, “Improvement of the photo-bias stability of the Zn-Sn-O field

effect transistors by an ozone treatment”, ECS 222nd Meeting, 7-12 October 2012, Honolulu, Hawaii. (accepted)

3. Conferences

3.1 International

1. Myung Soo Huh, **Bong Sop Yang**, Jae Won Song, Sang Jin Han, Seok Jun Won, Cheol Seong Hwang, and Hyeong Joon Kim, “Influence of low-pressure sputtering method on the properties of tin doped indium oxide thin films”, IC-MAP 2008, 18-20 August 2008, Je-ju, Korea.
2. **Bong Sop Yang**, Myung Soo Huh, Jae Won Song, Cheol Seong Hwang, and Hyeong Joon Kim, “Electrical property of $\text{Al}_2\text{O}_3/\text{SnO}_2$ MIS capacitor deposited by sputtering process”, ICMAP 2008, 18-20 August 2008, Je-ju, Korea.
3. **Bong Sop Yang**, Myung Soo Huh, Jae Won Song, Jeong Hwan Kim, Seok Jun Won, Cheol Seong Hwang, and Hyeong Joon Kim, “Influence of low-pressure process and rapid thermal annealing treatment on the electrical property of $\text{Al}_2\text{O}_3/\text{SnO}_2$ MIS capacitor”, 2nd IS-TCOs, October 22 - 26, 2008, Crete, Greece.
4. Myung Soo Huh, **Bong Sop Yang**, Jae Won Song, Jeong Hwan Kim, Seok Jun Won, Cheol Seong Hwang, and Hyeong Joon Kim, “Improved electrical characteristics of SnO_x thin-films deposited by low-pressure sputtering method”, 2nd IS-TCOs, October 22 - 26, 2008, Crete, Greece.
5. Jeong Hwan Kim, Tae Joo Park, Kwang Duk Na, Myung soo Huh, **Bong Sop Yang**, Hyeong Joon Kim and Cheol Seong Hwang,

"Influence of pre-deposition annealing and ozone treatment on the electrical property of $\text{HfO}_2/\text{SnO}_2$ MIS capacitor", 2nd IS-TCO 2008, Hersonissos, Greece, Oct. 22-26, 2008.

6. Myung Soo Huh, **Bong Seop Yang**, Seungha Oh, Seok-Jun Won, Jae Kyung Jeong, Cheol Seong Hwang, and Hyeong Joon Kim, "Aluminum Oxide Doped Tin Oxide Thin Film Transistors", AVS-MPA, 21-23 July 2009, Manchester, United Kingdom.
7. Myung Soo Huh, **Bong Seop Yang**, Seungha Oh, Je-Hun Lee, and Hyeong Joon Kim, "Improved Electrical Properties of Sputtered Tin Oxide Films as the Active Layer of Thin Film Transistor", ICMAP 2009, 20-25 September 2009, Busan, Korea.
8. Myung Soo Huh, **Bong Seop Yang**, Seungha Oh, Seok-Jun Won, Jae Kyung Jeong, Cheol Seong Hwang, and Hyeong Joon Kim, "Improvement in the Device Characteristics of Tin Oxide Thin-film Transistors by Adopting Ultralow-Pressure Sputtering", Electrochemical Society, 5-9 October 2009, Vienna, Austria.
9. Myung Soo Huh, **Bong Sop Yang**, Seungha Oh, and Hyeong Joon Kim, "Aluminum doped Tin Oxide based Thin Film Transistors", The 6th international tin-film transistor conference, 28-29 January, Egret Himeji, Japan.
10. Myung Soo Huh, **Bong Seob Yang**, Seungha Oh, Seok-Jun Won, Sang Jin Han, Cheoi Lae Roh, and Hyeong Joon Kim, "The surface morphological and electrical properties of ultralow-pressure sputtered tin doped indium oxide film", 2010 53rd SVC annual technical conference, 17-22 April, Orland, Florida, USA.
11. **Bong Seob Yang**, Myung Soo Huh, Seungha Oh, and Hyeong Joon Kim, "Influence of post-annealing conditions on the

performances of zinc tin oxide thin-film transistors”, 2010 53rd SVC annual technical conference, 17-22 April, Orland, Florida, USA.

12. **Bong Seob Yang**, Myung Soo Huh, Seungha Oh, Byung Du Ahn, J. Lee, Jong Hoon Kim, and Hyeong Joon Kim, “Influence of channel thickness of zinc tin oxide films on the performances of thin-film transistors”, The 7th AMF-AMEC, June 28- July 1, 2010, Je-ju, Korea.
13. Myeong Sook Oh, Myeong Soo Huh, **Bong Seob Yang**, Seong Ha Oh, and Hyeong Joon Kim, “Structural, Electrical, and Optical Properties of Molybdenum Oxides Deposited by Ultra-Low Pressure Sputtering” The 7th AMF-AMEC, June 28- July 1, 2010, Je-ju, Korea.
15. Myung Soo Huh, **Bong Seob Yang**, Seungha Oh, Byung Du Ahn, J. Lee, Jong Hoon Kim, and Hyeong Joon Kim, “Improved Surface Morphological Properties of Indium Tin Oxide films by Using Ultralow-pressure Sputtering Process” The 7th AMF-AMEC, June 28- July 1, 2010, Je-ju, Korea.
16. Seungha Oh, Myung Soo Huh, **Bong Seob Yang**, Hyeong Joon Kim, “Influence of annealing temperature, Zn/Sn ratio and O₂ partial pressure on the performances of zinc tin oxide thin-film transistors”, IUMRS-ICEM 2010, 22-27 August 2010, KINTEX, KOREA. (Poster)
17. Myeong Sook Oh, Myung Soo Huh, **Bong Seob Yang**, Jeong Hyun Moon, Do Hyun Lee, Seung Ha Oh, and Hyeong Joon Kim “Thermal and Electrical Characteristics of MoO₂/4H-SiC Shottky barrier Diodes” First international Conference on Materials for Energy, July, 2010

18. Myeong Sook Oh, Myeong Soo Huh, **Bong Seob Yang**, Seong Ha Oh, Jeong Hyuk Yim, Do Hyun Lee, Chang Hyun Kim, and Hyeong Joon Kim, "Comparison of MoO_x/4H-SiC Schottky contacts formed by annealing after reactive sputtering and oxidation annealing of molybdenum", 2011 MRS Fall Meetings & Exhibits, November 28 - December 2, 2011, Hynes Convention Center, Boston, MA
19. Ung Soo Lee, **Bong Seob Yang**, Myeong Sook Oh and Hyeong Joon Kim, "Experimental Characteristics of SiO₂ and Al₂O₃-ZrO₂ thin film layer for OLED moisture barrier", 2011 MRS Fall Meetings & Exhibits, November 28 - December 2, 2011, Hynes Convention Center, Boston, MA
20. Yoon Jang Kim, Bong Seob Yang, Seungha Oh, Jae Kyeong Jeong, Hyeong Joon Kim, "Effect of Annealing Temperature on the Electrical Characteristics of Solution Processed Zinc Tin Oxide Thin Film Transistors" Electrochemical Society, 6-11 May 2012, Seattle, USA.
21. Seungha Oh, **Bong Seob Yang**, Yoon Jang Kim, and Hyeong Joon Kim, "Composition Dependence of the Negative Bias Light Illumination Instability of Indium Zinc Oxide Transistors", ECS 222nd Meeting, 7-12 October 2012, Honolulu, Hawaii. (accepted)
22. **Bong Seob Yang**, Seungha Oh, Yoon Jang Kim, and Hyeong Joon Kim, "Improvement of the photo-bias stability of the Zn-Sn-O field effect transistors by an ozone treatment", ECS 222nd Meeting, 7-12 October 2012, Honolulu, Hawaii. (accepted)

2.2 Domestic

1. Myung Soo Huh, **Bong Sop Yang**, Jae Won Song, Cheol Seong Hwang, and Hyeong Joon Kim, “Improving the surface morphological and electrical properties of low-pressure sputtered ITO films”, 한국재료학회, 17 November 2008, Suwon, Korea.
2. **Bong Sop Yang**, Myung Soo Huh, Jae Won Song, Cheol Seong Hwang, and Hyeong Joon Kim, “Electrical property of Al_2O_3 deposited in low temperature by sputtering process”, 한국재료학회, 17 November 2008, Suwon, Korea.
3. Myeong Sook Oh, Myung Soo Huh, **Bong Seop Yang**, Do Hyun Lee, Jeong Hyun Moon, Seung Ha Oh, and Hyeong Joon Kim “Fabrication and Characterization of $MoO_x/4H-SiC$ Schottky barrier Diodes” 2010 한국반도체학술대회, 25 February 2010, Exco, Daegu, Korea.

3. Patents

3.1 Domestic (2 ea)

B. S. Yang et al., “Oxide-based Thin-film Transistors”, 2 ea

KR2008-0109060 : Thin-film Transistor and Fabricating Method of the Same

KR2009-0048665 : Fabricating Method of Metal Oxide Layer, Fabricated Thin-film Transistor Array Substrate Using the Same and Fabricating Method thereof

Abstract (in Korean)

최근 고화질 제품의 구현을 위하여 유연성 디스플레이와 평판 디스플레이가 많은 관심을 받고 있다. 비정질 산화물은 기존에 사용되어온 비정질 Si 에 비해 높은 이동도와 높은 투과율, 낮은 생산비용을 갖고 있기 때문에 차세대 박막트랜지스터의 채널 물질로 적용될 것으로 예측된다. 하지만, 빛과 전압이 가해질 때 발생하는 소자의 열화문제가 산화물 반도체의 실제 제품 적용에 큰 걸림돌로 작용하고 있다.

이러한 문제의 해결을 위해, 이 논문에서는 Zinc Tin Oxide (ZTO) 박막트랜지스터를 제작하여 광·전압 스트레스에 의해 변화되는 특성을 살펴보고, 여러 가지 실험적 변수의 조절을 통한 신뢰성 향상에 대한 연구를 진행하였다. 먼저 이 논문에서는 스퍼터링법으로 ZTO에 ZrO_2 를 첨가한 ZTZO 박막트랜지스터를 제작하였다. 박막 내에 ZrO_2 의 함량이 증가할수록 소자의 기본적인 특성은 열화 되었지만 박막트랜지스터의 광 신뢰성은 향상되었다. X-ray photoelectron spectroscopy (XPS) 분석을 통하여, ZTO 박막에 첨가한 ZrO_2 의 함량이 증가할수록 ZTZO 내부에 존재하는 산소 공공의 양이 줄어드는 것을 확인하였으며, 이러한 결과로 ZTZO 소자의 신뢰성이 향상되었다. 즉 빛에 의해 박막내부에 존재하는 산소공공이 여기 되며 전자를 공급하여 신뢰성의 열화를 일으키는 것을 확인하였다. 또한 표면의 photo-desorption mechanism 이 신뢰성 향상에 미치는 영향에 대해서도 연구하였다. 채널 표면에 존재하는 OH 결합의 정도에 따라 신뢰성 측정 중 빛에 의해 탈착 되는 산소의 양이 달라지게 된다. 따라서 초기 채널 표면에 존재하는 hydroxyl groups 의 양이 늘어날수록 신뢰성 특성이 향상되게 된다. 이를 통해 산화물 반도체의 광 전압 신뢰성에 채널의 표면 특성이 큰 영향을 미치는

것을 확인하였다. .

다음으로, ZTO 트랜지스터에 오존처리를 가할 경우 발생하는 광 신뢰성 특성 변화에 대해 연구하였다. 오존처리 시간이 길어질수록 소자의 광 신뢰성이 비약적으로 향상되었다. 표면과 내부의 화학상태에 대한 분석으로 XPS and Fourier transformed infrared (FTIR) contact angle analyzer (CA)을 진행하였다. 오존 처리 시간이 증가할수록 박막에 존재하는 산소 공공의 농도는 감소하였다. 이로 인해 신뢰성 측정 중 빛에 의해 여기 되는 산소 공공의 수가 감소함으로써 신뢰성이 향상된다. 또한 오존처리를 함으로써 표면에 존재하는 hydroxyl groups 의 양은 증가하고 상대적으로 표면에 흡착되어있는 산소의 양은 감소하게 되며 신뢰성 측정 중에 표면에서 탈착되는 산소분자의 수가 감소하고 신뢰성 특성이 향상된다.

마지막으로, 신뢰성 향상의 두 가지 메커니즘에 대한 상대적인 기여도를 확인하기 위해 Al_2O_3 와 polymer 를 사용, passivation 층을 적용한 소자를 제작하였다. 신뢰성 측정 결과 passivation 층을 적용한 소자에서 적용하지 않은 소자에 비해 약 85% ~ 90% 의 신뢰성 향상이 발생하였다. 이를 통해 표면에서의 산소 분자의 탈착이 신뢰성에 더 큰 영향을 미침을 확인하였다.

Keywords : Zinc Tin Oxide (ZTO), Zirconium oxide, field effect transistor, photo-bias stability, Negative bias illumination stability (NBIS), ozone treatment

Student ID : 2007-20722

Bong Seob Yang